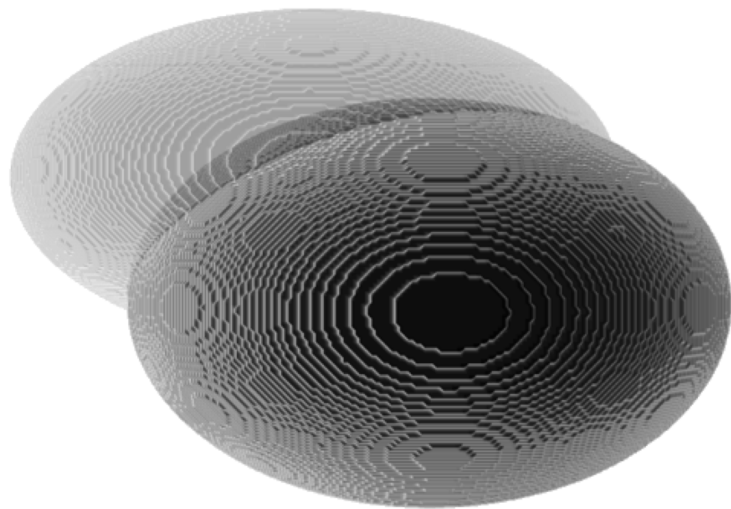


NUMERICAL SIMULATIONS OF CRYSTALLINE SAMPLES IN COHERENT
X-RAY DIFFRACTION IMAGING

SIGURD STENE



Investigating the effect of Bragg scattering

December 2022

ABSTRACT

This project aimed at finding the possible effects of Bragg scattering in coherent X-ray diffraction imaging (CDI). CDI is an imaging technique which allows for three-dimensional imaging with a resolution of tens of nanometer. Three-dimensional imaging has proven important in many fields, for example by quickly revealing the three-dimensional structure of viruses. In CDI, a sample is exposed to a bright and coherent beam, and its diffraction pattern is measured in the far-field limit. By oversampling the diffraction pattern and applying well-known phase retrieval algorithms, the sample can be reconstructed without the use of lenses, hence avoiding many of the limitations related to X-ray lenses. However, the method, originally developed for non-crystalline samples, assumes that all the incoming photons will be scattered to the low-frequency region of the corresponding Fourier space. For crystalline samples, there will be a significant signal also in the Bragg geometry, but this effect is not accounted for in today's reconstruction algorithms. During this project, these effects have been studied to see how severe the Bragg scattering is. This was done by calculating the diffraction pattern of a known object and simulating the intensity loss due to Bragg scattering by reducing the diffraction intensity for some projections. By applying sufficiently large reductions the reconstruction quality degraded significantly. This indicates that Bragg scattering might have an impact on real experiments as well, but before concluding, a further analysis, comparing the simulations against experimental data, would have to be conducted.

ACKNOWLEDGEMENTS

I would like to express my gratitude to my supervisors Basab Chattopadhyay and Dag Werner Breiby for giving me the opportunity to delve into the world of X-ray microscopy, steadily guiding me toward deeper insights.

I would also like to thank Daniyal Younas for always being open for questions.

Finally, a thanks goes out to Vincent Favre-Nicolin for writing the simulation tools used in this project, as well as taking the time to answer questions coming all the way from Norway.

CONTENTS

1	MOTIVATION	1
2	BACKGROUND INFORMATION	3
2.1	Introduction	3
2.2	X-ray Scattering	4
2.3	The Fourier transform	5
2.3.1	Properties of the Fourier Transform	5
2.4	Scattering geometries	6
2.5	Coherence	6
2.6	Brilliance	10
3	COHERENT DIFFRACTION IMAGING	11
3.1	Introduction	11
3.2	Phase Problem	11
3.3	Oversampling	13
3.4	Phase Retrieval Algorithms	14
3.4.1	Error Reduction algorithm	15
3.4.2	Hybrid Input-Output algorithm	16
3.4.3	Shrink wrap algorithm	16
4	METHOD	19
4.1	Introduction	19
4.2	Object generation	19
4.3	Diffraction	20
4.3.1	Ensuring sufficient oversampling	20
4.3.2	Simulating the diffraction pattern - Applying Bragg scattering	20
4.4	Reconstructing the objects	21
4.5	Error analysis	22
5	RESULTS AND DISCUSSION	25
5.1	Overview	25
5.2	Density distribution	26
5.3	Density distribution - averaged structure	30
5.4	Deviation from the initial structure	31
5.5	Further work	32
6	CONCLUSION	35
	BIBLIOGRAPHY	36

MOTIVATION

The ability to study the structure of materials is important to our understanding of their function. Be it a crack in a bridge, a pore in a biological sample or the morphology of nanoparticles, all structural information help us understand how materials function and how one can alter them to have more desired properties.

X-ray microscopy techniques allow for high resolution, three-dimensional imaging of samples ranging from viruses to integrated circuits [10, 21]. Other microscopy techniques, such as electron microscopy and atomic force microscopy, can provide better spatial resolution, but these have other limitations, e.g. being restricted to looking at the surface or only working for thin samples. X-rays, with their relatively weak interaction with matter, can be used to image thicker, three-dimensional samples without destroying the samples. This major advantage has been one of the main driving forces to develop X-ray imaging methods, and has led to the development of many different methods. Earlier, X-ray imaging techniques have been limited by the difficulty to make good optical elements for X-rays, with the best resolutions being around 10 nm [8, 27, 34]. Newer, lensless techniques, such as Coherent Diffraction Imaging (CDI), have been developed to overcome this limitation [25, 33]. Here, the lenses are exchanged with area detectors. These measure the scattered X-rays in the far-field Fraunhofer limit. By utilising that the diffraction pattern in the Fraunhofer limit is proportional to the square of the Fourier transform of the object, given that the incoming beam is coherent, one can reconstruct the object through an inverse Fourier transform. To achieve this, one first have to retrieve the phase information which is lost in the intensity measurements. This is done by performing a so-called oversampling of the diffraction pattern and utilising well-developed phase retrieval algorithms [2–5, 7, 13–18, 24, 28].

This project will focus on CDI, first envisioned by Sayre in 1952 [35] and proved experimentally by Miao et al. in 1999 [25]. CDI was first developed to image non-crystalline samples, before it later has been extended to crystalline samples. The non-crystalline nature of the samples result in a continuous diffraction pattern, which can easily be oversampled.

In theory, the resolution in CDI experiments is only limited by the wavelength of the X-rays, typically in the range of angstroms. However, the best recorded resolution is 2 nm in two dimensions [37], where strongly scattering silver nanocubes were examined, and 5 nm in three dimensions [26]. Typically, high resolution CDI results have a resolution around tens of nanometers [26]. In practice, it has been found that the resolution is limited by the maximal scattering vector one can measure [8]. For large scattering vectors, the signal to noise ratio is typically too low. Earlier, this was a problem for smaller scattering vectors as well, which partly explains the long development time from the method was envisaged in 1952, but with the development of third and fourth generation synchrotron facilities, the brightness of the X-ray beam has improved significantly. Today's fourth generation synchrotron facilities, such as the European Synchrotron Radiation Facility in Grenoble, France, can produce X-ray beams 10 trillion times brighter than medical X-rays. This has been necessary for the development of CDI and related methods. Both to achieve the required signal to noise ratio and also to produce an X-ray beam of well-defined coherence, which makes it possible to keep the phase information between all the constituents in the diffraction experiment.

One limitation to the CDI technique, is that the entire sample must be illuminated by the X-ray beam, limiting the possible samples to micrometer sized objects, due to the finite

size of the beam. Newer techniques, such as ptychographic CDI [33], can image extended objects by piecing together scans taken of different overlapping parts of the sample [32]. These techniques do however not have the same resolution as CDI. There also exist a wide variety of other CDI based techniques, such as Bragg CDI, which can be used to recover the strain structure of nanocrystals [8], and reflection CDI, where a surface can be studied with a sub-nanometer resolution [26].

One issue regarding CDI is that it assumes that all the incoming intensity will hit the detector in the small angle geometry. This is however not the case, as is readily measured in today's experiments, where wide angle detectors pick up a strong signal for crystalline samples [41]. In other words, Bragg scattering due to sub-resolution structures will reduce the intensity in the diffraction pattern for certain projections. The aim of this project is to look at the effects of this scattering. By understanding these effects, a future goal would be to incorporate them into future phase retrieval algorithms. In this project, the exploration of the effects will be done purely numerically, using simulation tools to generate diffraction patterns from a known object and then see how well the current reconstruction algorithms are able to reconstruct the object given a certain amount of intensity reduction for some of the projections. The methodology will be further explained in Chapter 4. First, a general introduction to the necessary theory needed to describe the phenomenon will be given in Chapter 2, starting with a short description X-ray scattering and the generation of coherent X-ray beams at today's third and fourth generation synchrotron facilities.

BACKGROUND INFORMATION

2.1 INTRODUCTION

X-rays are highly energetic electromagnetic radiation, with a typical energy between 100 eV and 100 keV, corresponding to wavelengths in the range of 0.01 nm to 10 nm, as illustrated in Figure 1. This range includes the size of atoms. Compared to other probes, X-rays interact rather weakly with most materials, resulting in a comparably large penetration depth. Adding this together, one is left with a excellent candidate that can be used to study the three dimensional structure of materials [1].

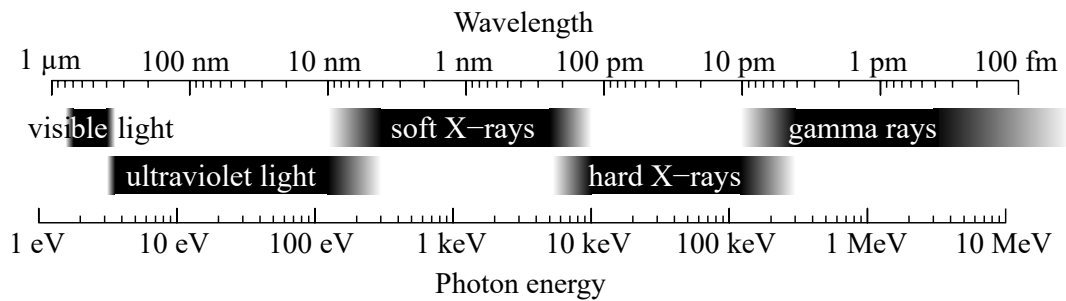


Figure 1: A comparison of the energy and wavelengths of X-rays and other types of radiation. X-rays cover the part of the spectrum equal to both atomic and mesoscopic structures. Adapted from Wikimedia commons.

Structural information can be found by looking at both the absorption and scattering of X-rays. The absorption techniques utilise that the absorption of X-rays scales as Z^4 , where Z is the atomic number. Hence, a contrast between different elements in a material can be found, which can be used to study the composition of the material. This is used in standard X-ray scans as well as in Computed Tomography, techniques which are commonly used to study the internal structure of the human body. A further discussion is however out of scope for this project, as the focus will be on X-ray scattering techniques instead. As will be shown below, the scattering techniques can be used to find both the atomic structure as well as the larger scale structures of materials. X-ray scattering is at the core of coherent X-ray diffraction imaging (CDI). Therefore, the next sections will be dedicated to an recapitulation of the theory behind X-ray scattering.

The X-rays used in CDI experiments are typically produced at synchrotron facilities, like the European Synchrotron Radiation Facility (ESRF) in Grenoble. A synchrotron is a particle accelerator, where electrons in vacuum are accelerated to relativistic speeds and forced to follow a circular path by a magnetic field [42]. The electrons are carried around large storage rings, the one at ESRF having a circumference of 844 meter, and the X-ray beam generation is done in tangential insertion devices called undulators. An undulator consists of many pairs of magnets, with alternating direction of the field. By introducing the electrons to this alternating magnetic field, the electrons start to oscillate and hence accelerate, creating electromagnetic radiation with a frequency corresponding to the frequency of the oscillation, as described by Maxwell's equations. This will yield a X-ray beam of sufficient quality to perform CDI experiments. What this means will be discussed in more detail in Section 2.5 and 2.6.

2.2 X-RAY SCATTERING

Scattering of X-rays can most easily be described as the interaction between the incoming X-rays and the electrons in the sample. The X-rays, which is an alternating electromagnetic field, will accelerate the electrons and new X-rays will be produced which will propagate in another direction [1]. As mentioned, this interaction is rather weak, allowing for a high penetration depth and the study of three-dimensional objects [26]. However, it also results in a weak signal, which can be difficult to interpret if the source is not sufficiently brilliant [38]. At this point it is important to note that the protons of a material also will be affected by the X-rays, but since their mass is more than 3 orders of magnitude larger than the electrons' mass, they will not be accelerated in the same manner, and the effect will be even weaker.

Two important quantities to describe X-ray scattering, and scattering in general, are the differential scattering cross section and the scattering length [1]. The differential scattering cross section is the probability that a single electron will be scattered by an incoming X-ray to a certain direction, given by a solid angle. It is given by

$$\frac{d\sigma}{d\Omega} = \frac{I_{sc}}{\Phi_0 \Delta\Omega}, \quad (1)$$

where I_{sc} is the scattered intensity, Φ_0 is the incident flux and $\Delta\Omega$ is the solid angle which the detector covers [1]. The scattering length of an atom is defined as

$$-r_0 f^0(\mathbf{q}), \quad (2)$$

where $r_0 = 2.82 \times 10^{-5} \text{ \AA}$ is the Thomson scattering length, also known as the classical electron radius, $f^0(\mathbf{q})$ is the atomic form factor, and $\mathbf{q} = \mathbf{k}' - \mathbf{k}$ is the scattering vector, where \mathbf{k} is the incoming wave vector and \mathbf{k}' is the wave vector of the scattered wave [1].

The form factor is defined as

$$f^0(\mathbf{q}) = \int \rho(\mathbf{x}) e^{-i\mathbf{q}\cdot\mathbf{x}} d\mathbf{x}, \quad (3)$$

where $\rho(\mathbf{x})$ is the electron density of the atom [1]. The form factor is thus dependent on the atomic number, where a larger atomic number means more electrons and a larger form factor.

When multiple atoms are present, the scattering amplitude is given by

$$F^{\text{molecule}}(\mathbf{q}) = -r_0 \sum_i f_j(\mathbf{q}) e^{-i\mathbf{q}\cdot\mathbf{x}_j}, \quad (4)$$

where $-r_0 f_j(\mathbf{q})$ is the scattering length of the j th atom, and \mathbf{x}_j is the position of the j th atom [1]. Here, molecule only means that there are multiple atoms present. It is thus a general term, which might include larger structures not normally considered as molecules.

The scattering intensity, which is what one measures in a diffraction experiment, can be shown to be proportional to the absolute square of the scattering amplitude [42], i.e.

$$I(\mathbf{q}) \propto |F^{\text{molecule}}(\mathbf{q})|^2. \quad (5)$$

As can be seen from Equation 3, the atomic form factor is essentially the Fourier transform of the atom's electron density, meaning that also the scattering intensity will be related to the Fourier transform of the object's electron density. This will be important later on when looking at the implementation of CDI. A short summary of the Fourier transform and its properties will therefore be given in the next section.

2.3 THE FOURIER TRANSFORM

The Fourier transform is a mathematical operation that transforms a function from the time domain to the frequency domain, or equivalently from the space domain to the spatial frequency domain [39]. In this work, only spatial frequencies will be considered, and the Fourier transform will be denoted by \mathcal{F} . The Fourier transform of a function $f(\mathbf{x})$ is defined as

$$\mathcal{F}\{f(\mathbf{x})\} = F(\mathbf{q}) = \frac{1}{(\sqrt{2\pi})^D} \int f(\mathbf{x}) e^{-i\mathbf{x}\cdot\mathbf{q}} d\mathbf{x}, \quad (6)$$

where \mathbf{q} is the spatial frequency vector, D is the dimension of the system considered and the integration is done over the entire space [39]. Equivalently, the inverse Fourier transform is defined as

$$\mathcal{F}^{-1}\{F(\mathbf{q})\} = f(\mathbf{x}) = \frac{1}{(\sqrt{2\pi})^D} \int F(\mathbf{q}) e^{i\mathbf{x}\cdot\mathbf{q}} d\mathbf{q}. \quad (7)$$

Throughout this project thesis the following notation will be used: Real space objects will be denoted by lower case letters, while their Fourier transform counterpart will be denoted with the corresponding upper case letter, as it is demonstrated in Equation 6 and 7.

When calculating the Fourier transform of an object function $o(\mathbf{x})$, the resulting Fourier space quantity $O(\mathbf{q})$ can be divided into two parts as shown below

$$O(\mathbf{q}) = |O(\mathbf{q})| e^{i\Phi(\mathbf{q})}, \quad (8)$$

where $|O(\mathbf{q})|$ is the amplitude, also known as the modulus, and $\Phi(\mathbf{q})$ is the phase of $O(\mathbf{q})$ [39]. Looking back at Equation 5, it can be seen that the scattering intensity is related to the squared modulus of an object's electron density. In other words, a scattering experiment only yields information about the amplitude of the Fourier transform of the object, and not the phase. This is known as the phase problem of crystallography and will be further discussed in Section 3.2.

In this project, a numerical implementation of the Fourier transform, known as the fast Fourier transform (FFT), will be used. FFT is a numerical algorithm that computes the discrete Fourier transform (DFT) of a function, in $O(n \log n)$ time, where n is the number of data points. The DFT in one dimension is defined as

$$F_k = \sum_{n=0}^{N-1} f_n e^{-i\frac{2\pi}{N}kn}, \quad (9)$$

where N is the number of data points, f_n is the n th data point, and F_k is the k th frequency component. The inverse DFT is defined as

$$f_n = \frac{1}{N} \sum_{k=0}^{N-1} F_k e^{i\frac{2\pi}{N}kn}. \quad (10)$$

Both of these will prove important when implementing CDI.

2.3.1 Properties of the Fourier Transform

Before proceeding with further scattering theory, some important properties of the Fourier transform will be listed [39]. These will be discussed further when they become relevant in the later sections.

1. The Fourier transform is linear:

$$\mathcal{F}\{Af(\mathbf{x}) + Bg(\mathbf{x})\} = A\mathcal{F}\{f(\mathbf{x})\} + B\mathcal{F}\{g(\mathbf{x})\}. \quad (11)$$

2. The Fourier transform of a shifted function is the same as the original function, multiplied by a phase factor:

$$\mathcal{F}\{f(\mathbf{x} + \mathbf{b})\} = e^{-i\mathbf{q}\cdot\mathbf{b}}\mathcal{F}\{f(\mathbf{x})\}. \quad (12)$$

3. The Fourier transform of a real function is symmetric around the origin:

$$\mathcal{F}\{f(\mathbf{x})\} = \mathcal{F}\{f^*(-\mathbf{x})\} = F(\mathbf{q}), \quad (13)$$

where $f^*(\mathbf{x})$ is the complex conjugate of $f(\mathbf{x})$. For real functions, $f^*(\mathbf{x}) = f(\mathbf{x})$.

4. The Fourier transform of a convolution between two functions is the product of the Fourier transforms of the functions:

$$\mathcal{F}\{f(\mathbf{x}) * g(\mathbf{x})\} = \mathcal{F}\{f(\mathbf{x})\}\mathcal{F}\{g(\mathbf{x})\} = F(\mathbf{q})G(\mathbf{q}). \quad (14)$$

2.4 SCATTERING GEOMETRIES

Having recapitulated the basics of the Fourier transform one can move on with the discussion on X-ray scattering. X-ray scattering experiments can be divided into two main categories, namely wide-angle (WAXS) and small-angle scattering (SAXS), as illustrated in Figure 2. The former, which is also known as Bragg diffraction, is used to study the atomic structure of materials, while the latter is used to study the morphology. As is known from Bragg's law [6], the scattering angle 2θ is related to the scattering vector \mathbf{q} by

$$\sin \theta = \frac{\lambda}{2d} = \frac{\lambda}{4\pi} |\mathbf{q}|, \quad (15)$$

where d is the interplanar spacing of the material [1]. From this, one can see that the scattering angle is inversely proportional to the interplanar spacing. This means that the signal registered at higher angles comes from smaller structures, while the signal at low angles comes from larger structures. At higher angles, one depends on the constructive interference from the scattered waves to achieve a strong enough signal. This means that the sample has to be somewhat crystalline for the scattered waves to interfere constructively.

SAXS does not require the sample to be crystalline, and is thus more versatile in many ways. It is however not able to resolve the smallest structures in a material. Since the measurements are done at small angles, the detector is typically placed far away from the sample to achieve a higher angular resolution. Today, one can achieve a resolution in \mathbf{q} of about $10 \times 10^{-3} \text{ nm}^{-1}$ [29]. CDI is inherently a SAXS technique, but in this project, the effects, if any, of the wide angle scattering will be studied.

2.5 COHERENCE

To take a step back, a short explanation of coherence will be given. A perfectly coherent wave is usually known as a plane wave. It is monochromatic and has a constant phase difference between different points in the wave, i.e. all the constituents of the wave travel in the same direction with the same velocity. A perfectly coherent wave is a theoretical concept not achievable in practice. Real beams are neither perfectly monochromatic nor do they propagate in one well defined direction. One can however create beams that come

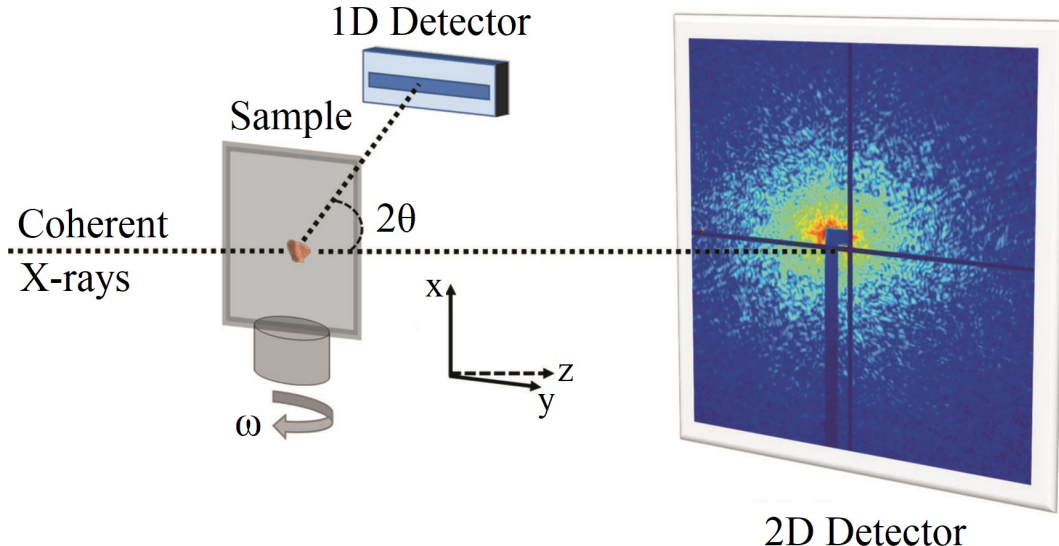


Figure 2: Illustration of the two main scattering geometries as performed in a CDI experiment. The two-dimensional detector measures the small angle scattering signal, while the one-dimensional, located at higher scattering angles, measures the wide angle signal. Adapted from [9].

close to the ideal. To put a number on the deviation from the ideal coherent wave, one can use quantities known as the longitudinal and transversal coherence length [1].

The longitudinal coherence length is a measure on how far two photons of slightly different wavelength can propagate before they are out of phase, assuming they were in phase to begin with. If they're out of phase at a distance given by the longitudinal coherence length, L_L , they will be in phase again at $2L_L$. The longitudinal coherence length can be approximated to

$$L_L = \frac{\lambda^2}{2\Delta\lambda}, \quad (16)$$

where λ is the wavelength of the photons and $\Delta\lambda$ is the bandwidth of the photons [1]. Here, $\Delta\lambda$ is assumed to be small, such that all the photons have approximately the same wavelength λ . With an incoming energy of 9 keV, having passed through a Si crystal monochromator for the (111) reflection, the transversal coherence length will be approximately 500 nm [44]. An illustration of the longitudinal coherence length is shown in Figure 3.

The transverse coherence length is a measure on how well the constituents of the beam travel in the same direction. This deviation might be caused by photons originating from different point sources. Huygens' principle says that each point in a wavefront might be seen as a point source, so any finite sized beam will inherently have some transversal coherence length related to it. Again, if they're out of phase at a distance L_T , where L_T is the transversal coherence length, they will be in phase again at $2L_T$. The transverse coherence length is given by

$$L_T = \frac{\lambda R}{2D}, \quad (17)$$

where D is the distance between the point sources and R is the distance from the point sources to the observation point [1]. R is assumed to be large compared to D , so that one can use the same value for the point sources. The transverse coherence lengths at third generation synchrotron sources are in the range of 3 to 500 μm [44], depending on their geometry. To perform coherent diffraction, the transverse coherence length has to be larger than the size of the sample [38].

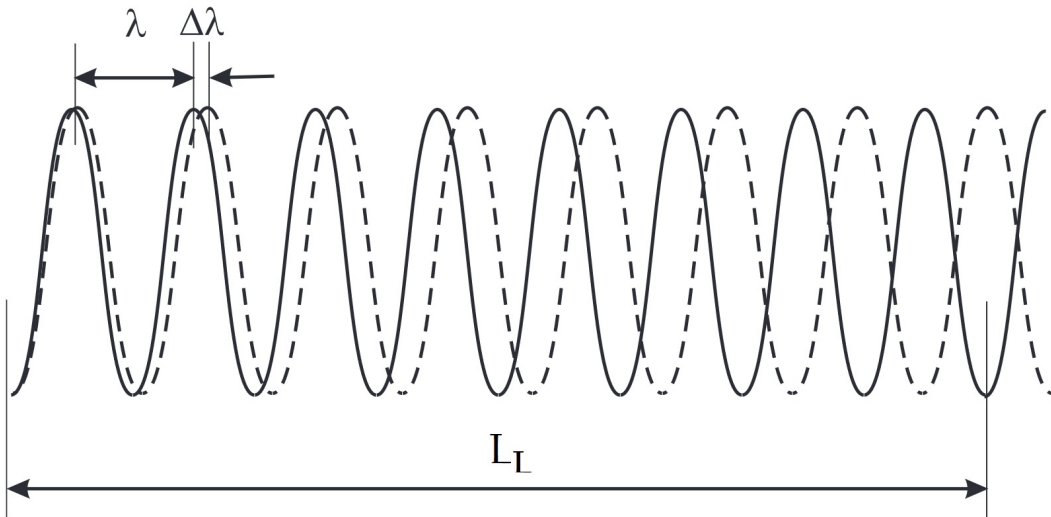


Figure 3: Illustration of the longitudinal coherence length. The two photons are in phase at $x = 0$, but out of phase at $x = L_L$. Illustration adapted from [38].

Collecting these terms together, one can look at a quantity known as the coherence volume. Although the coherence volume achievable in synchrotrons today is relatively large compared to traditional sources, it is still far from optimised. The next generation free-electron sources promise a coherence volume ten orders of magnitude larger [1].

From Equation 5 it can be shown that the intensity measured from a perfectly coherent beam is given by

$$I(\mathbf{q}) \propto \left| \sum_i f_j(\mathbf{q}) \right|^2. \quad (18)$$

The intensity is thus proportional to the square of the sum of the form factors [1]. This is due to the perfect correlation between the different constituents. For a perfectly incoherent beam, the cross terms in the sum will be completely uncorrelated, and the intensity will be given by

$$I(\mathbf{q}) \propto \sum_i |f_j(\mathbf{q})|^2. \quad (19)$$

The effects of this can be seen in Figure 4, where, it is shown that a coherent beam will result in a so-called speckle pattern. These speckles contain information about the positions of the objects, which is lost for an incoherent beam [38]. Said in other words, the diffraction intensity from an incoherent beam is the the sum of the diffraction intensities from the individual parts, meaning that the final diffraction pattern is completely unaffected by the interplay between them.

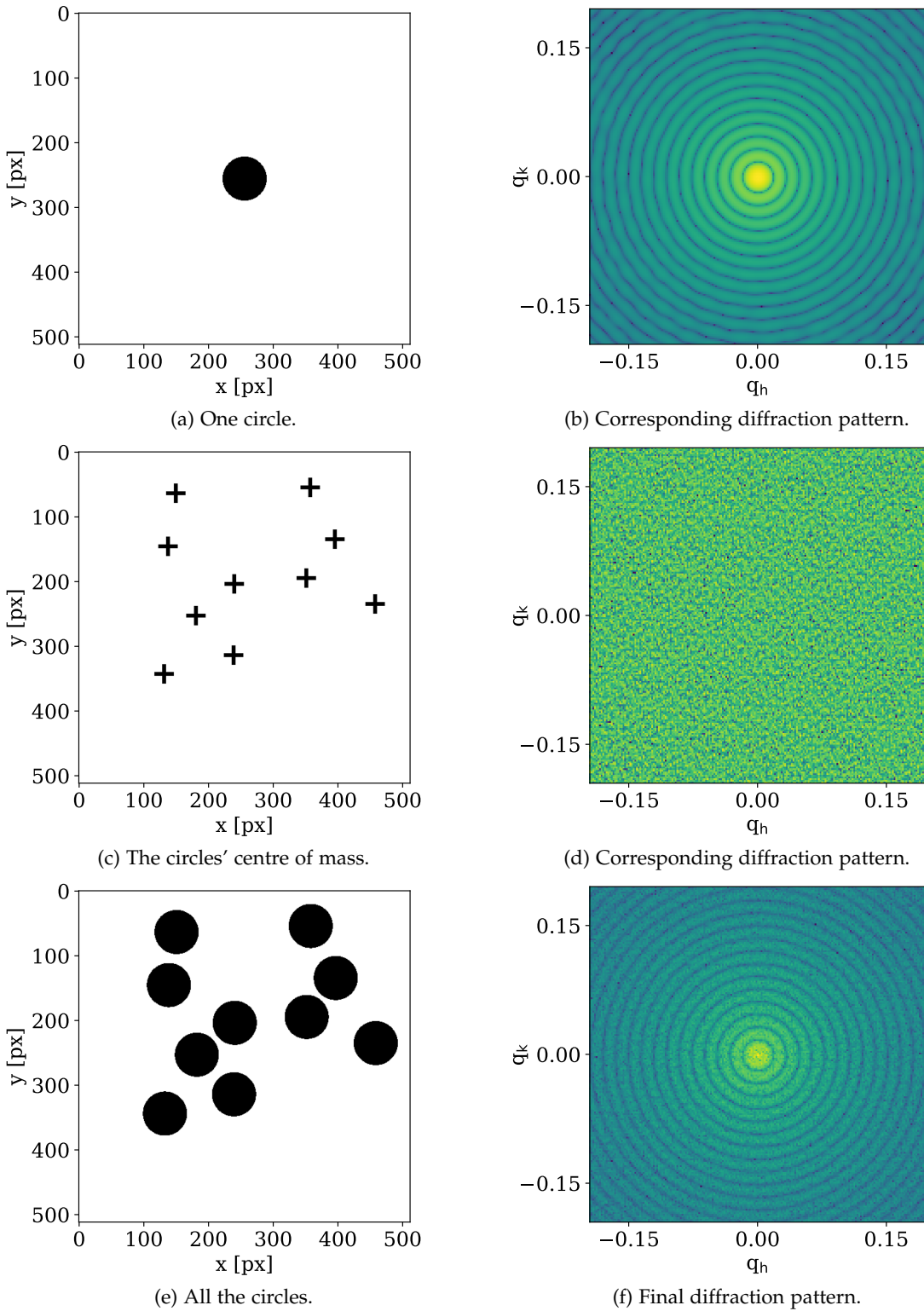


Figure 4: Simulated speckle pattern from 10 circles, where a perfectly coherent beam has been assumed. (a), (c) and (e) show the real space objects, while (b), (d) and (f) show their respective diffraction pattern. As can be seen, the final real space object might be seen as a convolution of one circle and a collection of positions. Following Equation 14, the diffraction pattern in (f) should be a multiplication of the patterns in Figure (b) and (d), which indeed is the case. If an incoherent beam had been assumed, the final diffraction pattern in Figure (f) would be equal the one in (b). Hence we see that the positional information of the circles would be lost. This is the critical information kept in the speckle pattern of Figure (d).

2.6 BRILLIANCE

In order to produce a beam of decent coherence, one must use a monochromator and apertures. The monochromator will reduce the bandwidth of the photons, resulting in a longer transversal coherence length, while the apertures will lower the divergence of the beam, hence minimising the transversal coherence length. This might result in a highly coherent beam, but the price to pay is a low intensity. By blocking out substantial parts of the beam, the intensity might end up being too low to be of any use. To overcome this, one must have a sufficiently intense source. All of these factors are important to consider when designing an X-ray beam, and they are collected in a term called the brilliance, which is a measure on the quality of the beam. The brilliance is given by

$$\text{Brilliance} = \frac{\text{Photons/seconds}}{(\text{mrad})^2 (\text{mm}^2 \text{ source area})(0.1\%\text{bandwidth})}, \quad (20)$$

where the numerator is the incoming intensity of the beam, mrad is a measure on the divergence of the beam and 0.1%bandwidth is the relative bandwidth compared to 0.1% [1]. From this one can see that a high brilliance is achieved by having a high intensity, a narrow beam with low divergence and a small bandwidth. All of which are desired properties of the beam. The reason one wants a high brilliance is that the scattering amplitudes are rather small for X-rays, and hence the signal to noise ratio is low. For third generation synchrotron sources, the brilliance is typically 10 orders of magnitude larger than traditional rotating anode sources. This has allowed for significant progress in the field of X-ray physics the last decades, and has been crucial for the development of CDI. The newer fourth generation sources are even better. Typically, two orders of magnitude better than the third generation sources.

3

COHERENT DIFFRACTION IMAGING

3.1 INTRODUCTION

As shown in the previous chapter, there is a close relation between the electron density of an object, $\rho(\mathbf{x})$, and the intensity of the measured diffraction pattern, namely that the scattering amplitude and therefore the measured intensity is related to the Fourier transform of the electron density. Unfortunately, one cannot simply apply an inverse Fourier transform to retrieve the electron density from the diffraction pattern. This follows from the measured intensity being proportional to the absolute square of the Fourier transform, hence not including the phase information. This is known as the phase problem of crystallography and will be further discussed in Section 3.2. However, what Sayre suggested in 1952 [35] and Miao et al. later proved experimentally in 1999 [25] was that one could retrieve the phase information in scattering experiments by performing a so-called oversampling in Fourier-space. The theoretical proof of this was given by Bates, Fright et al. in the early 1980s [2–5], and the practical phase retrieval algorithms were developed by Fienup et al. in the 1970s [13–18]. The concept of oversampling will be discussed more thoroughly in Section 3.3, while the reconstruction algorithms will be covered in Section 3.4.

3.2 PHASE PROBLEM

Before elaborating on the retrieval of the phase information through oversampling and phase retrieval algorithms, its importance will be briefly discussed. As mentioned above, and can be seen in Equation 5, the phase information is lost in the diffraction pattern. Hence, one cannot reconstruct the object through an inverse Fourier transform, even though one has all of the amplitude information.

To illustrate the importance of the phase, the Fourier transform of an image can be calculated before trying to reconstruct it by either swapping the phase or the amplitude with a random distribution, before performing the inverse Fourier transform. This will highlight how much of the information is kept in the phase, as illustrated in Figure 5 and 6. In Figure 5, the phase information has been exchanged with a random distribution. For this case, the reconstructed image does not resemble the original image in any apparent way, indicating that the amplitude information is not enough to reconstruct the image. The opposite case is shown in Figure 6, i.e. that the amplitude information has been exchanged. Here, one can see clear resemblances between the original and reconstructed image, motivating the need for a phase-retrieval process in CDI, as most of the information seems to be carried by the phase. This has also been shown by Oppenheim and Lim [31] and by Juvells et al. [22], who argued that the phase carries the most relevant information for most images, but that the amplitude could play a more important role for images with strong geometrical markers. Since most of the information is kept in the phase, it is crucial to retrieve this information if one wishes to reconstruct the object using an inverse Fourier transform. Luckily this can be done, as will be shown in the following sections.

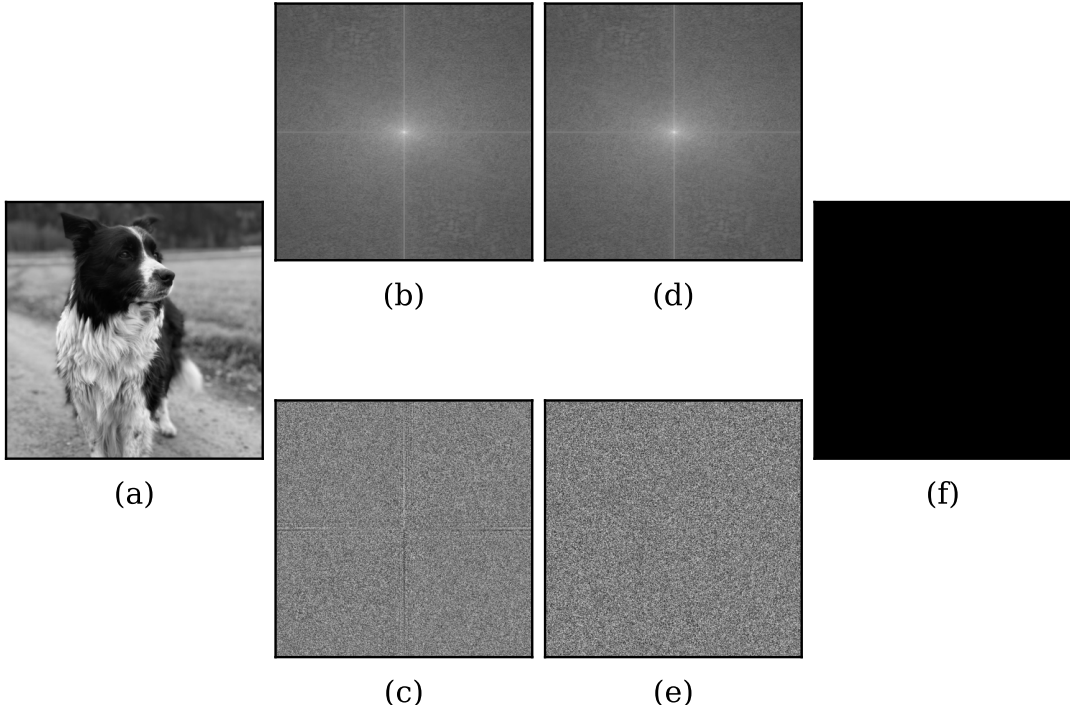


Figure 5: Reconstruction with a random phase. (a) is the original image. (b) and (c) is the amplitude and phase of the Fourier transform of the image, respectively. (d) is again the amplitude from the original image, while (e) is the average of the phase collected from an ensemble of images. (f) shows the result after performing an inverse Fourier transform with the amplitude from the original image and the random phase.

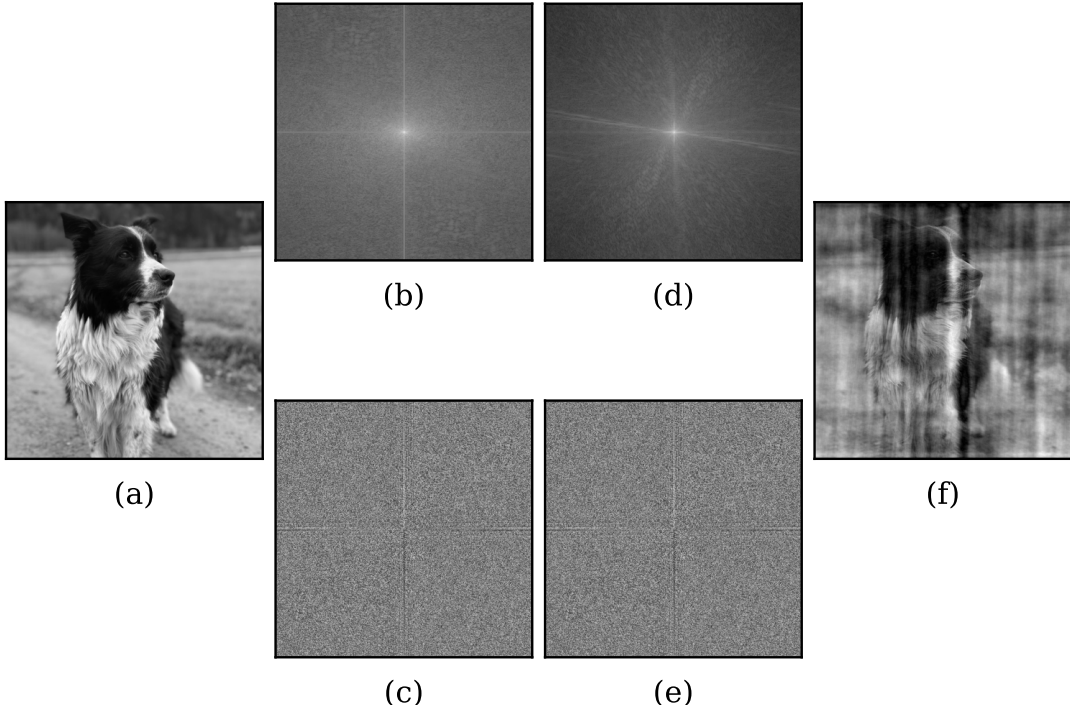


Figure 6: Reconstruction with a random amplitude. (a), (b) and (c) is the same as in Figure 5. Here, (d) is the average amplitude information from an ensemble of images, while (e) is the phase from the original image. Again, (f) is the result of an inverse Fourier transform using (d) and (e).

3.3 OVERSAMPLING

The fundamental criteria for phase retrieval is to perform a so-called oversampling in Fourier space. The oversampling criteria builds on the work of Whittaker [40], Nyquist [30] and Shannon [36], who showed that all bandlimited signals can be perfectly reconstructed if one samples them at a rate at least twice as high as the highest frequency. For materials, this translates to sampling the diffraction pattern at a frequency finer than the crystallographic sampling. This was Sayre's key insight from 1952 [35], who said that the phase could be retrieved if one sampled at a frequency of $1/2a$, where a is the length of an unit cell. This was further elaborated by Miao et al. in 1998 [28], who showed that the oversampling criteria was not as strict as previously thought. Instead of oversampling with a factor of two in every dimension, i.e. with a factor of eight for a three dimensional object, they showed that it is sufficient to oversample with a factor of $2^{1/D}$ in every dimension for real valued objects, where D is the dimension of the system. For complex valued objects, the chosen criteria was stricter, but still not as strict as previously thought.

The process of oversampling also works for non-crystalline samples. Here, one usually says that the sampling frequency should be twice as large as the Bragg density, where the Bragg density is defined as the density of Bragg peaks that would have been produced if the non-crystalline sample were turned into a crystal by repeating the structure with contact, but without overlap, in all directions [4, 28]. This equals the Bragg density of the autocorrelation function, which is what one measures in a scattering experiment. An illustration of this can be seen in Figure 7. The finer-than-Bragg criteria corresponds to oversampling the sample in real space as well [28]. This is given by the oversampling ratio, σ , defined as

$$\sigma = \frac{\text{electron density region} + \text{no-density region}}{\text{no-density region}}. \quad (21)$$

Following the discussion on the oversampling in Fourier space, it is clear that the oversampling ratio must be larger than 2. This is shown in Figure 8.

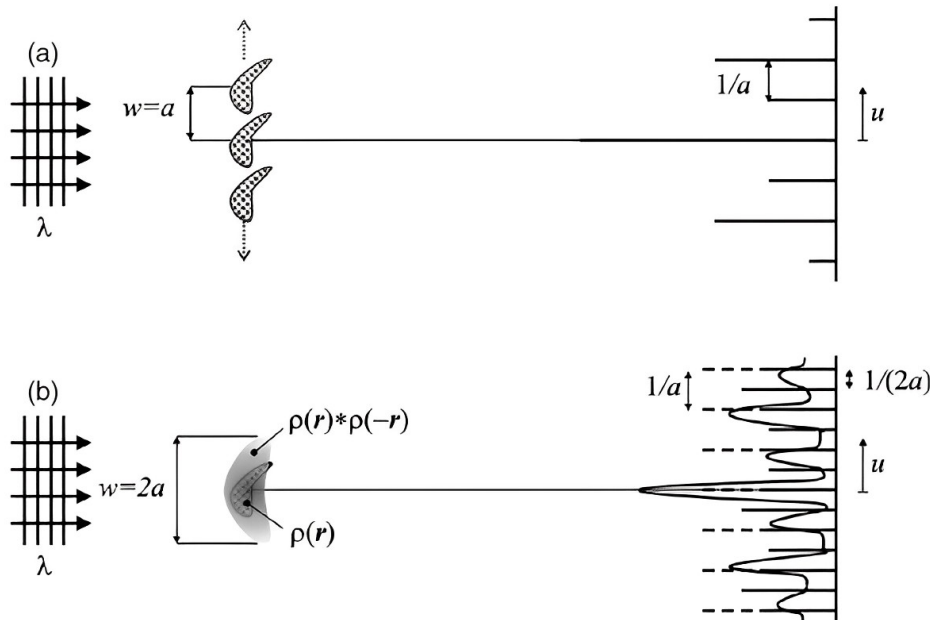


Figure 7: Illustration of the oversampling criteria. The Bragg density is given by assembling the initial structure into a perfect crystal. By sampling at a frequency twice as high as the Bragg density, equal to the Bragg density of the object's autocorrelation, one can retrieve the phase information. Adapted from [38].

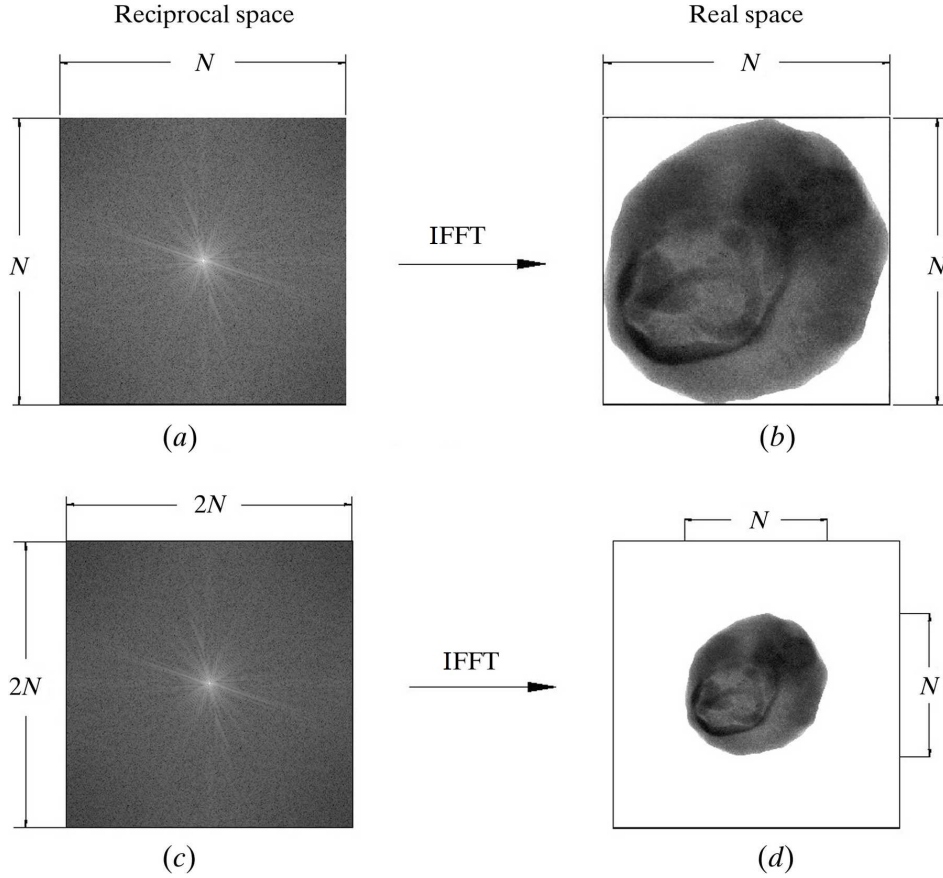


Figure 8: Illustration of how the oversampling in Fourier space corresponds to a higher oversampling ratio in real space. By sampling at twice the Bragg density, as done in (c), one will have a sufficiently large no-density area to retrieve the phase information, as shown in (d). Adapted from [28].

3.4 PHASE RETRIEVAL ALGORITHMS

As shown in Section 3.2, knowing the phase is crucial for the reconstruction of an object from Fourier space to real space. There are currently several algorithms available to overcome this problem. Some of the most common and easily implemented algorithms are the Error Reduction algorithm [14] and the Hybrid Input-Output algorithm [13, 14]. Both of these are iterative algorithms, where an initial guess on the phase is steadily improved to minimise the difference from the real phase. Gradient descent algorithms might also be used [14], and they are the basis of machine learning methods for phase retrieval, but none of these have been considered in this project due to the limited time schedule.

In general, it should be noted that the reconstruction algorithms are only able to decide the phase up to a constant phase factor. Adding a constant term to the phase will not change the solution, and the phase is therefore not uniquely determined. This is known as the uniqueness problem in phase retrieval. In general, if $o(x)$ is the actual solution, one cannot separate this from $o(x + x_0)\exp(i\phi_0)$, where ϕ_0 is a constant phase factor and x_0 is a shift in real space. For a real valued object, $o^*(-x + x_0)\exp(i\phi_0)$ will also be a valid solution for the phase retrieval problem. This follows from the shifting and centrosymmetric property of the Fourier transform, as described in Equation 12 and 13. $o(x)$, $o(x + x_0)\exp(i\phi_0)$ and $o^*(-x + x_0)\exp(i\phi_0)$ are known as the trivial characteristics of the phase problem of $o(x)$ [28]. They are trivial in the sense that they all represent the same object, just shifted or rotated in space. In other words, CDI is not able to retrieve the exact position or rotation of an object, but this is seldom of interest and could easily be found in other ways. One advantage with this, i.e. that CDI is not able to separate between different positions of the object, is that CDI

is unaffected by small sample vibrations during the diffraction experiment, thus making it more robust against experimental noise [26].

Apart from the trivial characteristics, it has been shown that the phase can almost always be decided uniquely for real and positive objects of dimension $D \geq 2$ [7, 20].

3.4.1 Error Reduction algorithm

The Fienup's Error Reduction algorithm (ER), which is a generalisation of the Gerchberg-Saxton algorithm originally used in electron diffraction imaging [13, 17, 18], is one of the simplest phase retrieval algorithms. It uses two constraints, one in real space and one in Fourier space, to iteratively find the phase of the object, $\Phi(\mathbf{q})$, from an initial guess, $\Phi_0(\mathbf{q})$, by performing forward and inverse Fourier transforms repetitively.

The first constraint is that the object lies within a volume S in real space known as the support. Additionally, the object is real and non-negative within this volume [13]. Outside this volume, the object function, $o(\mathbf{x})$, should vanish. The support can be decided by looking at the autocorrelation of the object. By using a diameter that is half the size of the largest diameter of the autocorrelation, one can ensure that the object is fully encapsulated within the support. This follows from the properties of the autocorrelation, which necessarily is at least twice as large as the object itself. The autocorrelation can easily be calculated since it is just the inverse Fourier transform of the square of the Fourier modulus, which is essentially what one measures in a diffraction experiment. This follows from Equation 14 by setting the two functions equal to each other.

$$\mathcal{F}^{-1} \left\{ |\mathcal{F}\{o(\mathbf{x})\}|^2 \right\} = \mathcal{F}^{-1} \{ O(\mathbf{q})O(^*\mathbf{q}) \} = o(\mathbf{x}) * o(-\mathbf{x}). \quad (22)$$

where the last term is the autocorrelation of the object, yielding a limit to how large it can be. This is however not a very tight constraint, and can lead to slower convergence [14]. Newer methods allow for an update of the support as more information about the object is found further out in the reconstruction process [24, 43]. It is also possible to use other a priori information about the object if that is available.

The second constraint, i.e. the Fourier constraint, is based on the measured intensity. When performing the forward Fourier transform, the calculated amplitude is exchanged with the measured amplitude, $|O(\mathbf{q})|$. The method is summarised below [14].

1. Choose random initial phase $\Phi_0(\mathbf{q})$, which yields
 $O_0 = |O(\mathbf{q})|\exp(i\Phi_0(\mathbf{q}))$.
2. Perform inverse Fourier transform to estimate the object function $o(\mathbf{x})$:

$$o'_n(\mathbf{x}) = \mathcal{F}^{-1} \{ |O(\mathbf{q})|\exp(i\Phi_n(\mathbf{q})) \}. \quad (23)$$

3. Apply the real space constraint:

$$o_{n+1}(\mathbf{x}) = \begin{cases} o_n(\mathbf{x})' & \text{if } \mathbf{x} \in S, \\ 0 & \text{if } \mathbf{x} \notin S. \end{cases} \quad (24)$$

4. Perform Fourier transform to estimate $O(\mathbf{q})$:

$$O'_{n+1}(\mathbf{q}) = \mathcal{F}\{o_{n+1}(\mathbf{x})\}. = |O_{n+1}(\mathbf{q})|\exp(i\Phi_{n+1}(\mathbf{q})). \quad (25)$$

5. Apply Fourier space constraint:

$$O_{n+1}(\mathbf{q}) = |O(\mathbf{q})|\exp(i\Phi_{n+1}(\mathbf{q})). \quad (26)$$

6. Repeat Points 2, 3, 4 and 5 until convergence, i.e.

$$o_{n+1}(x) = o_n(x) \text{ and } |O'_n(\mathbf{q})| = |O(\mathbf{q})|. \quad (27)$$

Typically, the mean square error in Fourier space is used to determine convergence. It is defined as:

$$\epsilon_n = \frac{\int_V |O_n(\mathbf{q}) - O(\mathbf{q})|^2 d\mathbf{q}}{\int_V |O(\mathbf{q})|^2 d\mathbf{q}}, \quad (28)$$

where V is the volume of the measured reciprocal space.

It has been proven that the squared error between $|O_n(\mathbf{q})|$ and $|O(\mathbf{q})|$ will decrease or at worst stay the same for each iteration. This is the reason why the algorithm is called the Error Reduction algorithm. Typically, the error will decrease rapidly initially, before flattening out [13, 14]. Another known problem with the ER algorithm, is that it usually converges to a local minimum instead of a global minimum. It might also end up in a state where the reconstructed object is a combination of the actual object and its centrosymmetric inversion, following the centrosymmetric property of the Fourier transform as described in Equation 13.

3.4.2 Hybrid Input-Output algorithm

The Hybrid Input-Output algorithm (HIO) was developed by Fienup et al. [13] to speed up the aforementioned convergence problem of the Error Reduction algorithm. The HIO differs from the Error Reduction algorithm by altering the real space constraint in Step 3 by using a negative feedback loop to minimise the mean square error in Fourier space. There are multiple implementations of the HIO algorithm, but one common presented by Fienup [13] exchanges the real space constraint with the following:

$$f_{n+1}(x) = \begin{cases} f'_n(x) & \text{if } x \in S, \\ f_n(x) - \alpha f'_n(x) & \text{if } x \notin S, \end{cases} \quad (29)$$

where α is a constant that determines the amount of negative feedback. Fienup mentioned that a combination of different constraints gave the best results. Fienup also proved that the HIO algorithm is fairly resilient against noise, keeping the low frequency information intact even at relatively high noise levels.

Despite the similarities between the algorithms, HIO doesn't suffer from many of the same drawbacks as ER. However, it might have problems reaching a minimum, so one usually switches to another algorithm, such as ER, when HIO has stabilised around some value. One might also use variations of the HIO algorithm, such as the detwinning HIO algorithm. In this variant, the support is halved along a direction every iteration to overcome the possible problem of centrosymmetric twins [16, 19].

3.4.3 Shrink wrap algorithm

As mentioned in Section 3.4.1, there exist methods to automatically update the support of the object during the reconstruction process. The shrink wrap algorithm (SW), developed by Marchesini et al. [24], is one such method. It is a modification of the HIO algorithm, where the support is updated around every twentieth iteration. By updating the support, one will eventually end up with a so-called "tight support", i.e. a support that is as close to the exact object shape as possible [23]. The support is updated by thresholding, i.e. removing the outer parts of the support where the reconstructed object is below a certain value, which is often taken to be relative to the maximum value of the reconstructed object.

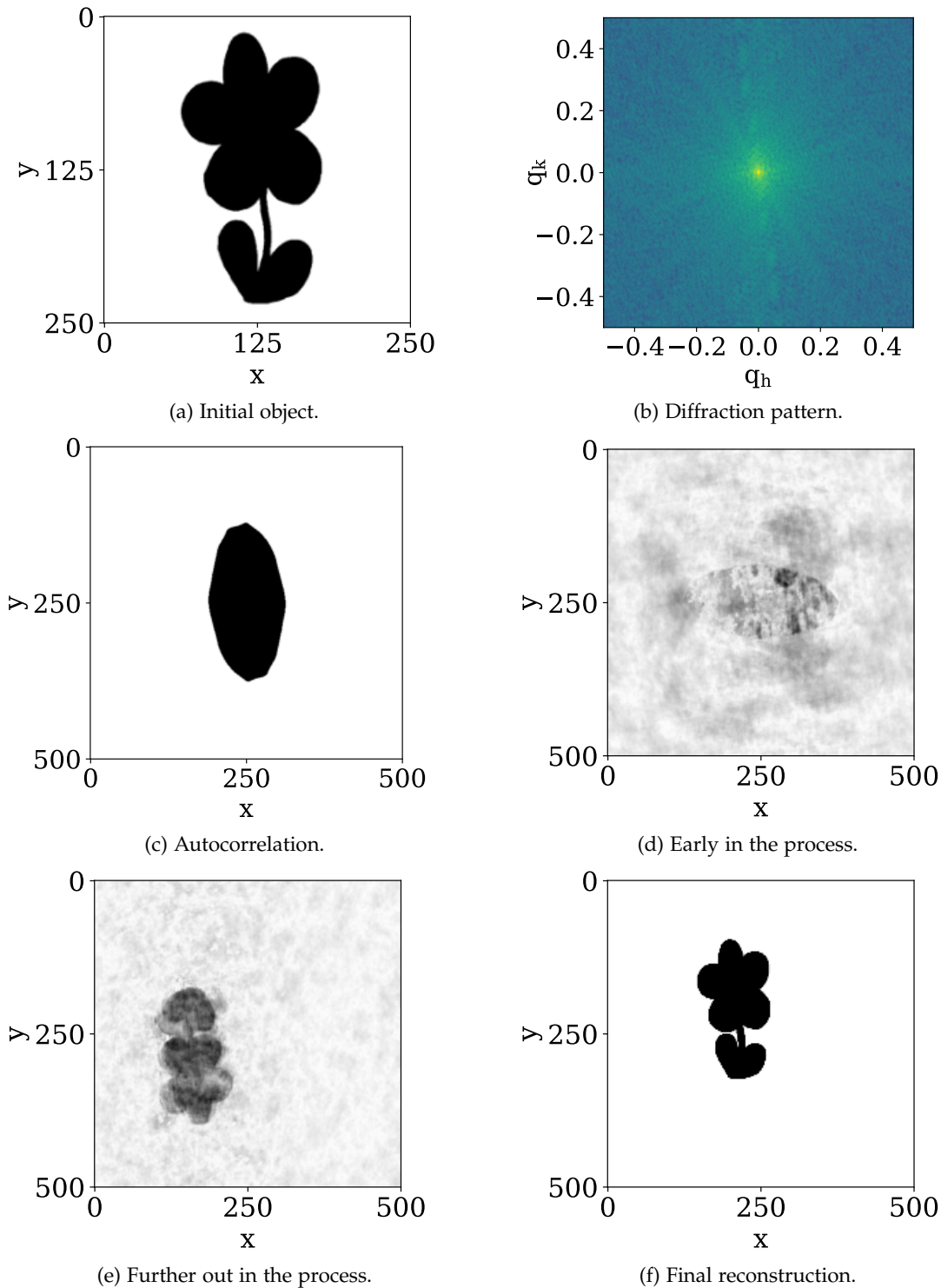


Figure 9: Illustration of the reconstruction process in CDI. (a), (b) and (c) show the initial object, its diffraction pattern and its autocorrelation, which was used as the initial support, respectively. (d) shows the reconstructed object after performing 5 iterations of the HIO algorithm, while (e) shows the reconstructed object after 6 shrink wrap iterations, where one shrink wrap iteration contained 20 HIO iterations followed by a support update. Lastly, the final result can be seen in (f). Here, 20 SW iterations and 20 ER iterations have been performed. The oversampling ratio was 2 in both directions, indicated by the initial matrix being twice as small as the rest. The different rotation of the object follows from the properties of the Fourier transform, as described in Section 2.3.1. The length scales are given in pixels.

METHOD

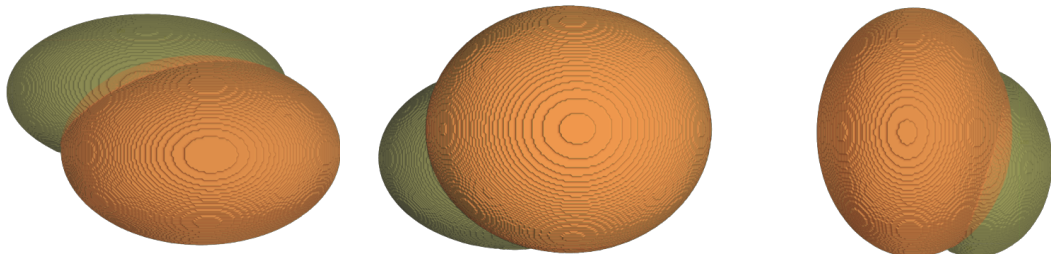
4.1 INTRODUCTION

In this project, the effects of Bragg scattering on CDI reconstructions have been analysed. To do this, an initial object was created digitally, before the diffraction pattern of this object was simulated. Then, the intensity for some of the projections were reduced, before the object was reconstructed again. Finally, the deviations from the initial object was studied. The details of this will be explained in the following sections.

4.2 OBJECT GENERATION

The examined object consisted of two overlapping ellipsoids. It was constructed digitally using Python. The two ellipsoids had different sizes and densities, where the orange ellipsoid in Figure 10, i.e. the lower one in Figure 10a, had a relative density of 1, and the green ellipsoid had a relative density of 0.8. The ellipsoids were created within a matrix of $256 \times 256 \times 256$ voxels. The details of the structure can be found in Table 1, and three overview images can be seen in Figure 10.

There were multiple reason for choosing two overlapping ellipsoids. Firstly, ellipsoids are simple objects that are easy to construct digitally. Secondly, by altering the length of the half-axes, one can create other common structures, such as disks, rods and spheres. Thirdly, the diffraction pattern of ellipsoids contains fewer high frequency components than other simple objects, such as cubes. This means that more of the information is kept in the low frequency components, which is what one measures in CDI. Of course, an object constructed digitally will consist of many small cubes, each giving rise to a high frequency component in the diffraction pattern, but the overall morphology is better kept for an ellipsoid than for a cube. Lastly, by examining two objects of different densities, one could see how well the density distribution was preserved in the reconstructions.



(a) The initial object viewed from the front. (b) The initial object viewed from the bottom. (c) The initial object rotated and viewed from the right.

Figure 10: The initial object viewed from three different directions. The orange area has a relative density of 1, while the green has a relative density of 0.8.

Table 1: Details of the object that was examined in this project. Centre is defined in relative coordinates compared to the system size of $256 \times 256 \times 256$ voxels. The size of the ellipsoids are given as a tuples containing the half-axes for ellipsoids, in the x, y and z direction, respectively. These are also given relative to the system size. For the overlapping parts, the ellipsoid with the lowest density was removed.

Description	Part	Rel. density	Size	Centre
Orange	1	1.0	(0.25,0.32,0.37)	(0.57,0.51,0.61)
Green	2	0.8	(0.22,0.27,0.40)	(0.41,0.43,0.47)

4.3 DIFFRACTION

To simulate the diffraction process, the python package PyNX, developed by Favre-Nicolin et al. [11, 12], was used. A further introduction to the package can be found in [12] and at <http://ftp.esrf.fr/pub/scisoft/PyNX/>. Perfect conditions were assumed under the diffraction simulation, i.e. a perfectly coherent beam, no beam stop or other imperfections of the experimental set up. This was done to focus on the effect of the intensity reductions. In order words, removing factors that might affect the reconstruction process, and thereby making it more difficult to compare the results.

4.3.1 Ensuring sufficient oversampling

To ensure a sufficient degree of oversampling, as described in Section 3.3, the diffraction pattern was sampled with twice as many voxels in each dimension as compared to the initial $256 \times 256 \times 256$ grid, i.e. $512 \times 512 \times 512$ voxels. This means sampling with a frequency of $1/(2 \times \text{system size})$, where the system size is the size of the initial grid in voxels. This degree of oversampling was significantly higher than required, since the diffraction pattern was sampled at a factor which is larger than two times the size of the object in every direction.

4.3.2 Simulating the diffraction pattern - Applying Bragg scattering

To calculate the diffraction pattern, the scattering amplitude of each part of the object was calculated, so that they later could be added together and squared to get the diffraction intensity, as shown in Equation 18. Before this, the scattering amplitude of certain projections for certain parts of the objects was reduced. By applying this reduction to only certain parts of the sample, one could simulate the situation of having a partly crystalline sample, or a sample where the crystalline parts were oriented in different directions. In this project, the sample was assumed to consist of two single crystalline domains, i.e. one domain per ellipsoid. Additionally, it was assumed that they only fulfilled the Bragg condition once, and that they fulfilled it at an angle of 20° compared to each other. The reduction itself was done by applying a two-dimensional filter to the three-dimensional scattering amplitude matrix. This was done along the z-axis of the array, so that the z-axis of the simulations corresponds to the z-axis of a real experiment, as shown in Figure 2. An example of an applied filter can be seen in Figure 11. Here, a intensity reduction of up to 10% has been applied. The reduction decreases from the maximum to zero following a normal distribution. This was assumed because of the broadening of the Bragg peaks, which allows the neighbouring projections to fulfil the Bragg condition to some extend.

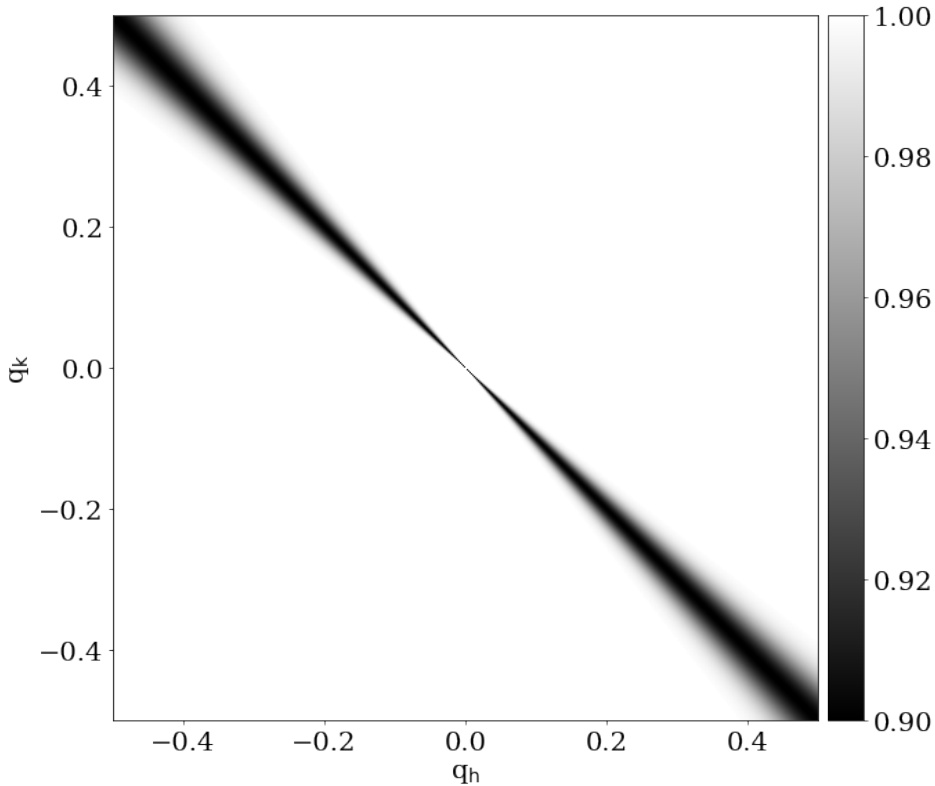


Figure 11: Illustration of a filter that was applied to the diffraction pattern to simulate the reduction in intensity due to Bragg scattering. Here, a 10% reduction would have been applied.

The reduction is a reduction in intensity. This means that if it is said that an intensity reduction of 10% has been applied, it is really a $\sqrt{10}\%$ that have been applied to the scattering amplitude, which later have been squared to get the intensity, and thus having an intensity reduction of 10%. In total, 9 different intensity reductions were applied, namely 0%, 5%, 10%, 15%, 20%, 30%, 40%, 50% and 60%, all having the same shape of the reduction filter as the one shown in Figure 11.

After having reduced the scattering amplitude for some of the projections, they were added together and squared to get the overall intensity. The intensity was then normalised to 10^{10} photons to improve the reproducibility of the reconstruction process and to better be able to compare the effect of the different reductions, as the density of the reconstructed objects scaled with the intensity of the diffraction pattern.

4.4 RECONSTRUCTING THE OBJECTS

To reconstruct the objects from the diffraction patterns, the same Python package as mentioned in Section 4.3, PyNX, was used. To initialise the reconstruction, a suitable support had to be decided. This was chosen to be a sphere with a radius that was known to be larger than the sample by looking at the autocorrelation function as described in Section 3.3. The support was later periodically updated using a function of the software, similar to the algorithm described in Section 3.4.3. To reconstruct the objects, a combination of the different algorithms described in Section 3.4 were used. More precisely, 150 iterations of the HIO algorithm, with a support update every 25th iteration, were applied, before 24 iterations of the detwinning HIO algorithm were used. Then 400 iterations of the HIO algorithm with a support update every 25th iteration were performed. Finally, 400 iterations of the ER algorithm, again with a support update every 25th iteration, were applied.

This algorithm was chosen because it provided reasonable reconstructions within reasonable time limits. A further analysis comparing different reconstruction algorithms were outside the scope of this project.

To have representative reconstruction data, 10 reconstructions were done for each intensity reduction parameter. In contrast to a real experiment, where one typically chooses a collection of the best reconstructions, all the reconstructions were kept for the following error analysis. This was done to see the entire impact of the intensity reductions on the reconstruction quality, so as to not hide the most inaccurate results. Also, for such a simple sample, without any defects in the diffraction process except from the Bragg scattering, it was assumed that the reconstruction algorithm should converge.

4.5 ERROR ANALYSIS

To analyse the reconstruction quality, multiple quantities were examined. This was done with multiple Python scripts, which can be found at https://github.com/SigurdStene/TFY4520_autumn22. The first quantity that was examined was the density distribution of the reconstructed objects. This was done by fitting two Gaussian functions to the density data, and comparing the mean, μ , and standard deviation, σ , of the two distributions. These values will be referred to as μ_h , σ_h , μ_l , and σ_l , where the subscript h and l refers to the high and low density regions, respectively. Additionally, an extra subscript might sometimes be used, for example μ_{h10} , to indicate which intensity reduction parameter was used, here exemplified by a reduction of 10%. In order to fit these Gaussian functions, the density data was first binned into 500 bins. The same bins were used for all the reconstructions. All the values were calculated based on the 10 reconstructions for each intensity reduction parameter, i.e. by first calculating the value for each reconstruction and then finding the final value by looking at the mean. The uncertainties are given by the standard deviation from this process.

The ratio between the two means, μ_l/μ_h , was calculated to see how well the densities of the initial object had been kept in the reconstructions. This was then compared to the ratio of the initial distribution of 0.8, as given in Table 1. Additionally, the ratio between the area under the two distributions was calculated. These values will be referred to as r_μ and r_a , respectively. To calculate r_a , the area under the two Gaussian distributions were compared. These were found from the known integral of a Gaussian distribution, which is given by:

$$\int_{-\infty}^{\infty} ae^{-\frac{(x-\mu)^2}{2\sigma^2}} dx = a\sqrt{2\pi\sigma^2}, \quad (30)$$

where a is the maximum value of the distribution. Hence, one can look at the ratio between the areas as:

$$r_a = \frac{\int_{-\infty}^{\infty} a_h e^{-\frac{(x-\mu_h)^2}{2\sigma_h^2}} dx}{\int_{-\infty}^{\infty} a_l e^{-\frac{(x-\mu_l)^2}{2\sigma_l^2}} dx} = \frac{a_h \sqrt{2\pi\sigma_h^2}}{a_l \sqrt{2\pi\sigma_l^2}} = \frac{a_h \sigma_h}{a_l \sigma_l}. \quad (31)$$

An example of a fitted distribution is shown in Figure 12.

To minimise the effect of random fluctuations in the density distribution, the average reconstructed objects were also analysed. To calculate these, all the reconstructions per intensity reduction parameter were aligned as best as possible, before their average was calculated. The mean objects, as they will be referred to from now, were then analysed in the same way as the individual reconstructions.

The second quantity that was examined was the deviation from the initial structure. To do this, the mean objects were normalised. This was done by dividing them by their respective μ_h value. The deviation from the initial structure was analysed in by aligning the mean reconstructed objects with the initial object, and subtracting them from each other.

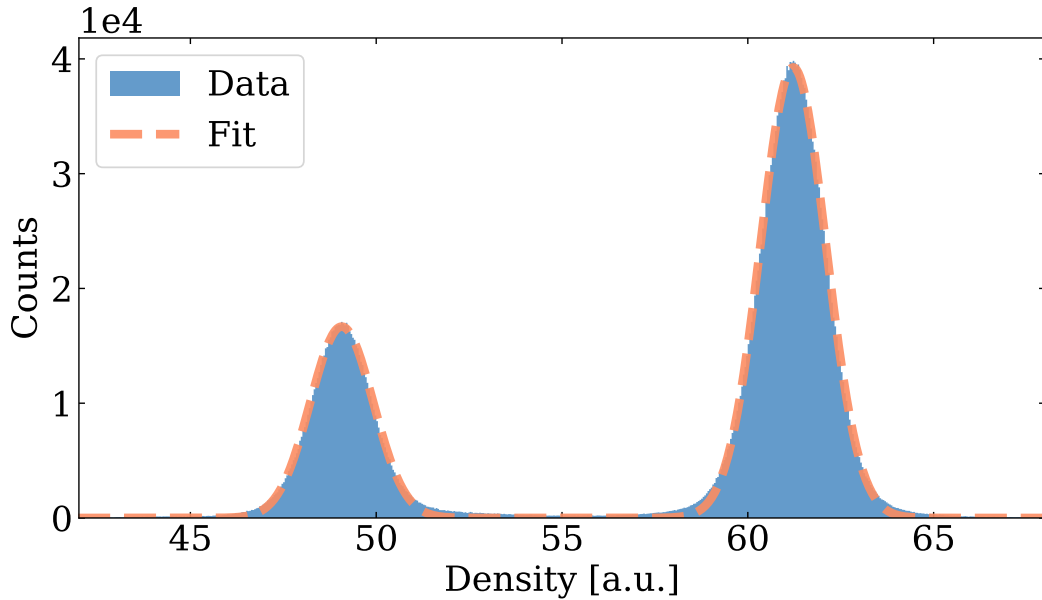


Figure 12: Example of two Gaussian functions which have been fitted to the density distribution of an reconstructed sample.

RESULTS AND DISCUSSION

5.1 OVERVIEW

To get an overview of the results, images of the reconstructed objects were analysed. For intensity reductions of less than 40%, the reconstructions were qualitatively the same as the initial object. For larger reductions, deviations from the initial object were common, for example in the form of additional material appearing outside the original structure. These additional areas often had a relatively low density, and could thus have been filtered out easily. However, without any a priori information about the object, it would not have been possible to decide if these were artefacts or not.

Six examples of the reconstructed objects are shown in Figure 13 and 14. In the former, only the shape of the reconstructed object is considered, while the latter includes the density as well. Both figures show the general trend in the data. For low reductions, exemplified with two 0% reductions in Figure 13a and 14a, both the shape and density partitioning were well kept. As the intensity reduction increased, the density gradually deviated more from the initial structure, as shown in Figure 14b. Finally, for the highest reductions, the shape of the reconstructed objects could also deviate substantially from the initial structure, exemplified in Figure 13c and 14c, as opposed to the good reconstruction in Figure 13b.

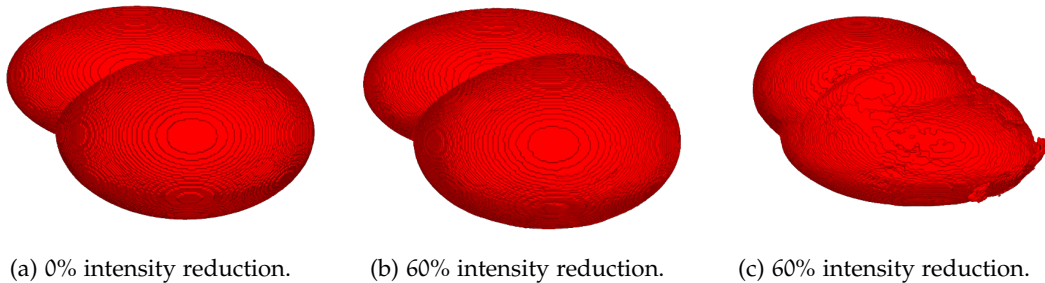


Figure 13: Reconstructions of the two ellipsoids for different intensity reductions. (a) and (b) were similar to the initial object shown in Figure 10, while (c) was qualitatively different from the initial object. In the latter, the ellipsoids were deformed and extra material had appeared. Note that (c) is the centrosymmetric inversion of (a) and (b).

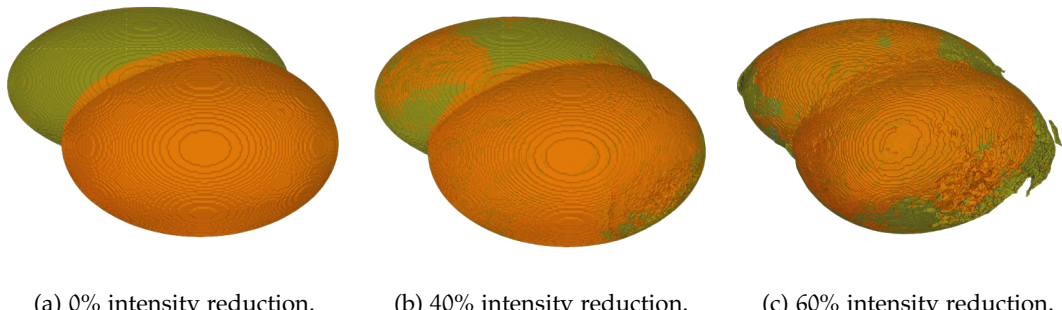


Figure 14: Three examples of reconstructions with density the density information included. As in Figure 10, orange and green indicate high and low density, respectively. (a) corresponds well with the initial object. (b) has kept the overall shape, but not the density distribution. (c) has neither kept the shape nor the density distribution.

5.2 DENSITY DISTRIBUTION

A more quantitative picture of the results can be found by looking at the density distribution of the reconstructed objects, as described in Section 4.5. This is shown in Figure 15. The figure shows how the width on the density distribution increased with increasing Bragg scattering, i.e. applied intensity reduction. The standard deviation of the two Gaussian functions increased from $\sigma_{l_0} = 0.78$ and $\sigma_{h_0} = 0.84$ for the reconstructions with no intensity reduction, to $\sigma_{l_{15}} = 0.99$ and $\sigma_{h_{15}} = 1.04$ for the reconstructions with a 15% intensity reduction and further to $\sigma_{l_{30}} = 1.91$ and $\sigma_{h_{30}} = 2.06$ with a reduction of 30%. This corresponds to an increase of 27% and 145% for σ_l and an increase of 24% and 145% for σ_h , respectively. For the lowest intensity reductions, i.e. 5% and 10%, the standard deviation of the Gaussian functions were almost the same as for no intensity reduction. All the values are listed in Table 2. The uncertainties in Table 2 are given by the standard deviation of the values from the 10 reconstructions for each intensity reduction, as described in Section 4.5.

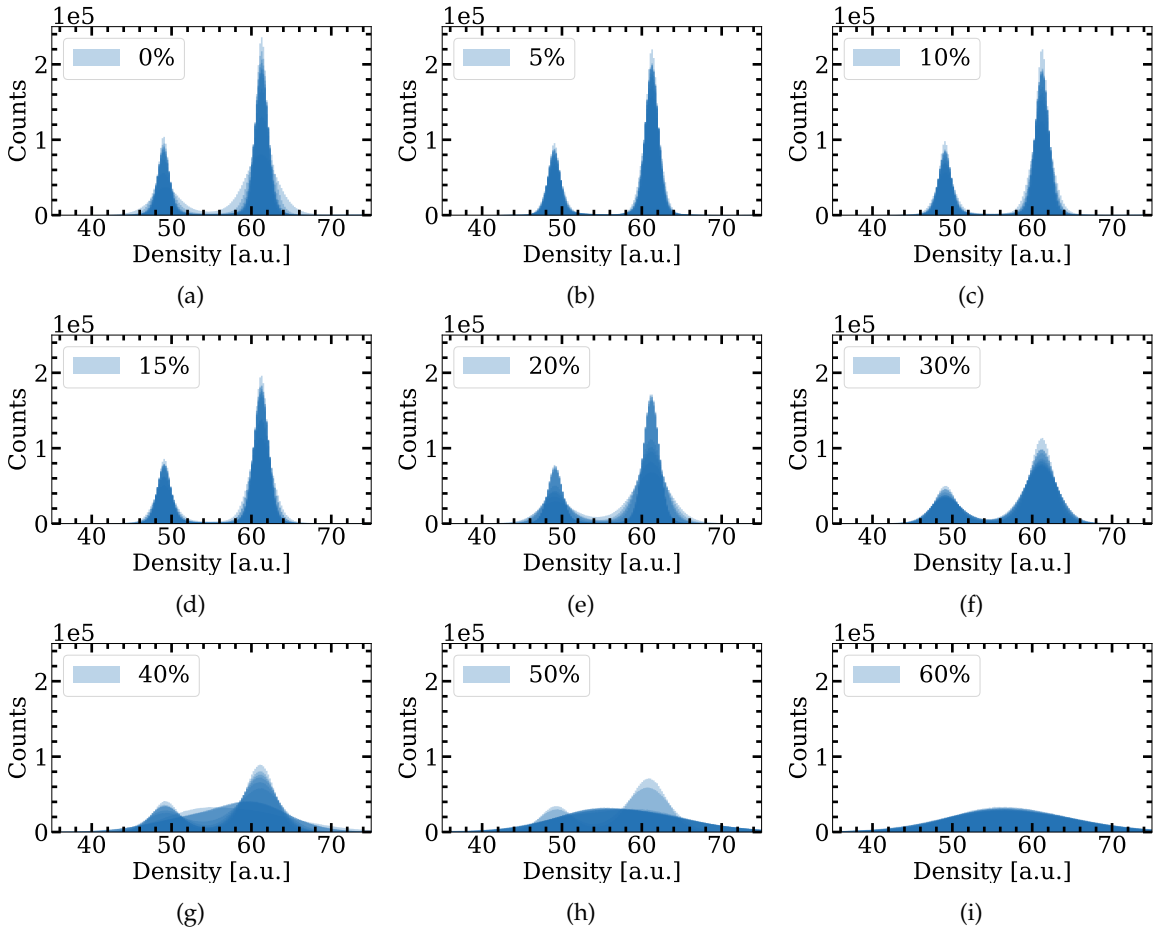


Figure 15: The density distributions for all the intensity reduction parameters. The intensity reduction is shown within the legend, as to indicate the colour of one single density distribution. For each parameter, the density distribution for the ten reconstructions are shown. As evident in the figure, the distributions became gradually wider with increasing intensity reductions. For the highest reductions, the two initial distributions were no longer separable for some of the reconstructions. Each distribution has the same colour, meaning that the darker colours stem from overlapping distributions.

Table 2: Mean and standard deviation of the density distributions for different intensity reduction parameters. For reductions larger than 30%, it was not always possible to separate the high density area from the low density area, resulting in a significant increase in the uncertainties. All the values are given in arbitrary units.

Int. red.	μ_l	μ_h	σ_l	σ_h
0%	48.99 \pm 0.01	61.28 \pm 0.01	0.78 \pm 0.07	0.84 \pm 0.08
5%	49.03 \pm 0.01	61.26 \pm 0.01	0.82 \pm 0.04	0.87 \pm 0.04
10%	49.04 \pm 0.01	61.24 \pm 0.00	0.80 \pm 0.10	0.84 \pm 0.11
15%	49.06 \pm 0.01	61.22 \pm 0.00	0.99 \pm 0.12	1.04 \pm 0.13
20%	49.17 \pm 0.03	61.16 \pm 0.03	1.41 \pm 0.30	1.47 \pm 0.29
30%	49.22 \pm 0.04	61.09 \pm 0.03	1.91 \pm 0.33	2.06 \pm 0.29
40%	50.56 \pm 2.60	59.91 \pm 2.33	3.37 \pm 1.36	3.27 \pm 0.94
50%*	52.04 \pm 5.01	56.98 \pm 3.23	5.10 \pm 2.24	4.62 \pm 2.24
60%*	46.98 \pm 7.94	56.51 \pm 3.03	5.51 \pm 2.11	6.41 \pm 2.40

The ratio between the mean of the low density voxels and the mean of the high density voxels, $r_\mu = \mu_l / \mu_h$, is shown in Table 3. It should be 0.8, as this was the ratio between the densities of the two parts in the initial object. The ratio between the volume of the two parts of the initial object, denoted by r_a , is also listed in Table 3. This should be 2.34, as the initial object had a distribution of 887 348 voxels with a relative density of 0.8 and 2 080 310 voxels of relative density 1. From Table 3, it can be seen that the ratio between the means of the two parts of the reconstructed objects is close to 0.8 for all intensity reductions, but with a significant increase in the uncertainty for reductions larger than 30%. This is also evident in Figure 15, where all the reconstructions for intensity reductions less than 40% qualitatively follow the same distributions, while some of the reconstructions for the larger reductions are qualitatively different from the others. For the largest reductions, the two parts were not always separated, resulting in a large uncertainty for all the quantities described there.

Table 3: The maximum values of the Gaussian functions, a_l and a_h , are given in arbitrary units. Their values are divided by 10^4 compared to the raw data in Figure 15, to make the values more readable. The values for r_μ and r_a were calculated from the a_l and a_h value for each reconstruction, i.e. not calculated from the a_l and a_h values in this table, explaining the differences in their uncertainties. For the largest intensity reductions, marked with *, this simple analysis failed, since the two parts of the initial objects were no longer separable.

Int. red.	a_l	a_h	r_μ	r_a
0%	10.35 \pm 0.98	23.35 \pm 2.48	0.80 \pm 0.00	2.44 \pm 0.04
5%	9.78 \pm 0.43	22.53 \pm 1.10	0.80 \pm 0.00	2.43 \pm 0.04
10%	10.17 \pm 1.13	23.66 \pm 2.72	0.80 \pm 0.00	2.44 \pm 0.04
15%	8.26 \pm 0.94	18.99 \pm 2.33	0.80 \pm 0.00	2.43 \pm 0.03
20%	6.01 \pm 1.24	13.82 \pm 2.75	0.80 \pm 0.00	2.41 \pm 0.02
30%	4.48 \pm 0.69	9.82 \pm 1.36	0.81 \pm 0.00	2.38 \pm 0.03
40%	3.02 \pm 0.82	6.11 \pm 2.46	0.85 \pm 0.08	2.25 \pm 0.73
50%*	2.53 \pm 1.90	3.54 \pm 2.85	0.92 \pm 0.13	-0.34 \pm 3.52
60%*	0.76 \pm 2.21	3.81 \pm 1.79	0.84 \pm 0.16	-1.56 \pm 14.68

Another way to study the density distribution is to look at two dimensional slices of the reconstructed objects. This is shown in Figure 16, where two reconstructions are shown, one from a reduction of 0% and one from a reduction of 40%. The reconstruction where no intensity reduction was applied had a clear separation between the areas with low and high density. This separation was less clear with increasing intensity reduction, exemplified with the 40% reduction reconstruction in Figure 16b.

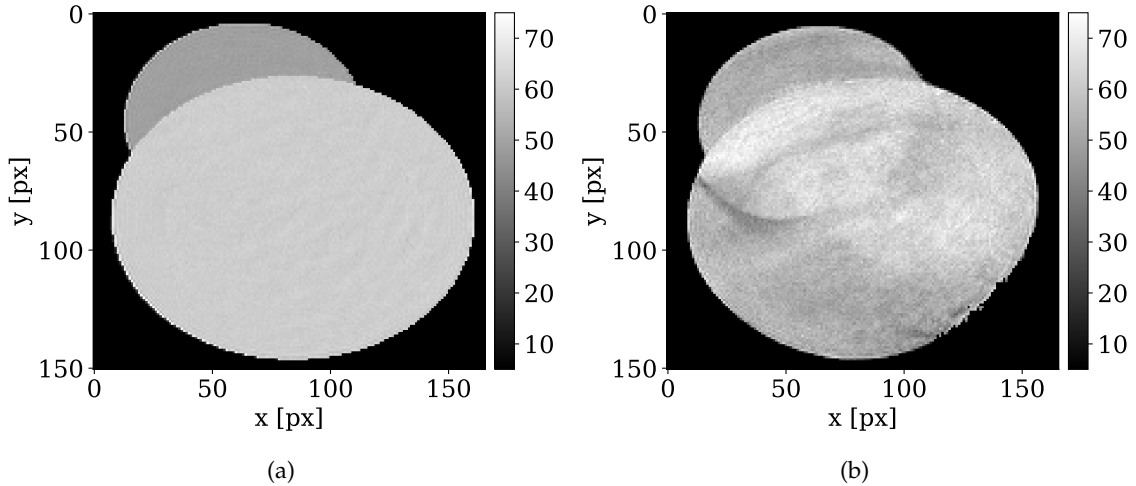


Figure 16: Density distribution of two reconstructions for two different intensity reductions, namely no reduction in (a) and 40% reduction in (b).

The same two-dimensional slice of the initial object is shown in Figure 17a. This was very similar to the reconstructed object with no intensity reduction shown in Figure 16a, and does not contain the same local variations as the reconstructed object with a 40% intensity reduction in Figure 16b. The differences between these deviations are shown in Figure 17b, where the relative densities of the voxels along a line of the two-dimensional slices are plotted as a function of their position. The figure shows how the reconstructed object with no intensity reduction followed the initial object well, while the reconstructed object with a 40% reduction varied a lot, sometimes having a relative deviation from the initial object of 20%.

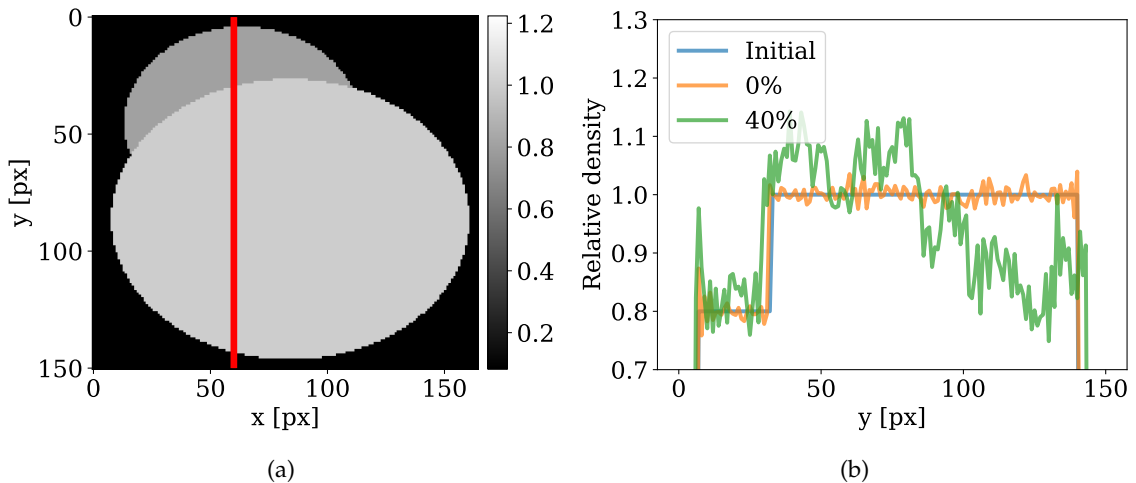


Figure 17: The local deviations through an one-dimensional slice of the sample. (a) shows the initial object and the line where the measurements were made. (b) shows the result. The data was collected from the slices shown in Figure 16. To compare the reconstructions with the initial data, the reconstructions had to be normalised, as described in Section 4.5.

These local variations are impossible to see by just looking at the shape of the reconstructed objects, but are important for the inner structures of materials. This might be wrongly interpreted as areas actually having a lower or higher density, i.e. either a different chemical composition or a different physical structure. Therefore, even though the reconstruction algorithm used in this project was able to reproduce the overall shape and density distribution of the objects for most of the intensity reductions, there still is a visible quality degradation, represented by the increasing width of the distributions when increasing the amount of Bragg scattering. Whether this degradation could have been avoided by averaging over several reconstructions have been studied in Figure 18. The figure shows a similar plot as Figure 17, but along a different line and including information from all the reconstructions from the chosen intensity reduction parameters. The intensity reductions that were included are 0%, 20% and 40%. For each intensity reduction, the relative densities for the 10 reconstructions along this line were collected. The mean and standard deviation of these are shown in the figure. The centre of the lines are the mean values, while their thickness is given as two times the standard deviation. The mean and standard deviation were calculated at every voxels, explaining the difference in the thickness of the lines. Again, the deviation increased with increasing intensity reduction, but not as much as in Figure 17b. The differences between no reduction and the lower reduction, i.e. 20%, were small, with the former being slightly more stable than the latter. From the figure, it is also clear that the objects were not aligned perfectly, as there is a large uncertainty at the edges.

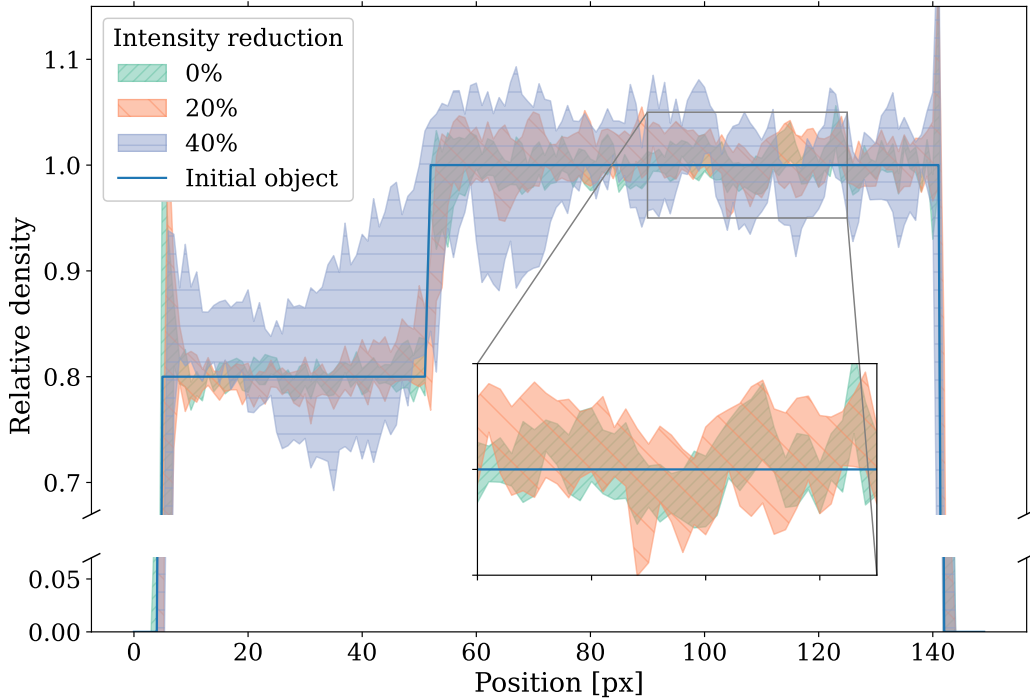


Figure 18: Illustration of the local variations from the initial structure. The inset figure shows the differences between no reduction and 20% reduction in more detail. Here, the upper and lower border corresponds to a five percent deviation, i.e. a relative density value of 1.05 and 0.95, respectively.

5.3 DENSITY DISTRIBUTION - AVERAGED STRUCTURE

This section presents the same main results from the section above, i.e. the density distributions, but for the mean structure. Figure 19 shows the density distribution for the mean reconstruction for the six lowest intensity reduction parameters. The three highest intensity reduction parameters were not included, as the reconstruction quality was too poor to align the reconstructed objects properly. The figure shows that the mean reconstructions have a narrower distribution than the individual reconstructions, as expected. This is also shown in Table 4, where the parameters from the fitted Gaussian functions are listed. In comparison to the values listed in Table 2, the standard deviation of the Gaussian functions were halved, proving that the reconstruction quality is improved by averaging the reconstructions. However, the same trend seen in Table 2 was still visible, i.e. the standard deviation increased with increasing intensity reduction. This does not apply for the 5% and 10% intensity reduction, but this was likely due to the one relatively bad reconstruction that was made after not applying any intensity reduction. This bad reconstruction is easily visible in Figure 15a. In other words, the trend where the reconstruction quality decreases with increasing intensity would likely be applicable for all the intensity reduction parameters if enough reconstructions were made.

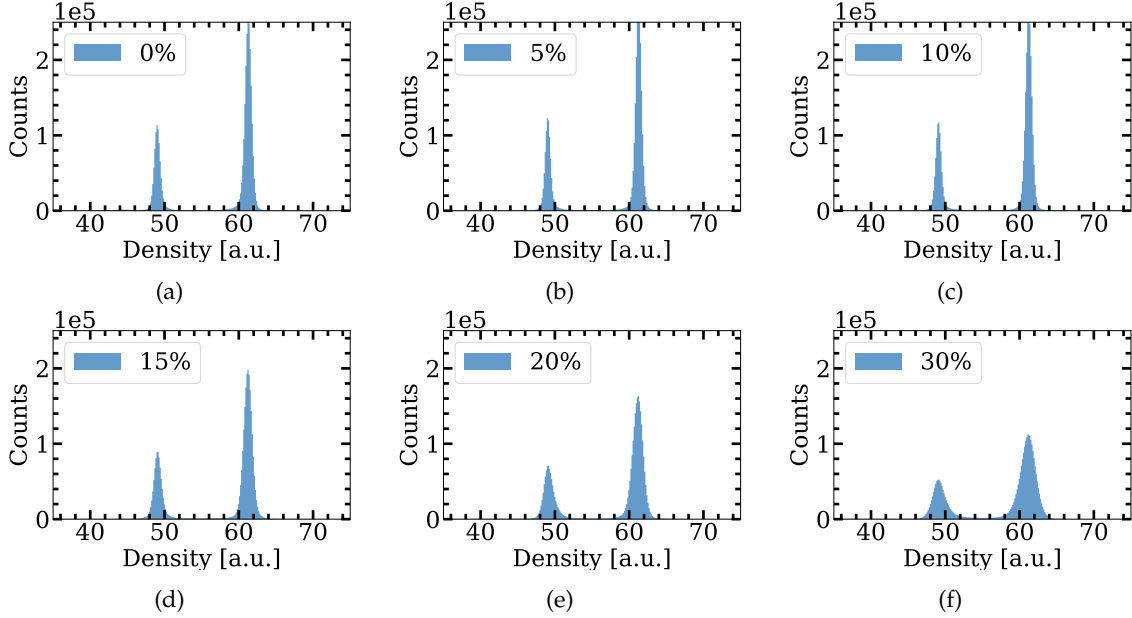


Figure 19: The density distributions of the average of the reconstructed objects for all the intensity reduction parameters. .

Table 4: Mean and standard deviation of the mean density distributions for different intensity reduction parameters. All the values are given in arbitrary units.

Int. red.	μ_l	μ_h	σ_l	σ_h
0%	49.02	61.28	0.41	0.44
5%	49.05	61.27	0.37	0.40
10%	49.09	61.24	0.39	0.43
15%	49.08	61.23	0.52	0.57
20%	49.16	61.17	0.67	0.70
30%	49.15	61.15	0.91	1.03

5.4 DEVIATION FROM THE INITIAL STRUCTURE

To further study the quality of the reconstruction, the overall deviation between the initial and the mean reconstructed objects were calculated. This is plotted in Figure 20. There were also some voxels with a relative deviation close to one, due to misalignment of the initial object and the mean reconstructions, but these were not included in the figure. The figure shows how the relative deviation increased with increasing intensity reduction, again omitting the fact that the mean object for the 0% intensity reduction was slightly worse than the 5% and 10% intensity reductions. The deviation was typically less than 2%, which is a high reconstruction quality. At the same time, there was a significant increase in the deviation from the 0% reconstruction and the 30% reconstruction, indicating the negative effects of Bragg scattering on the reconstruction results.

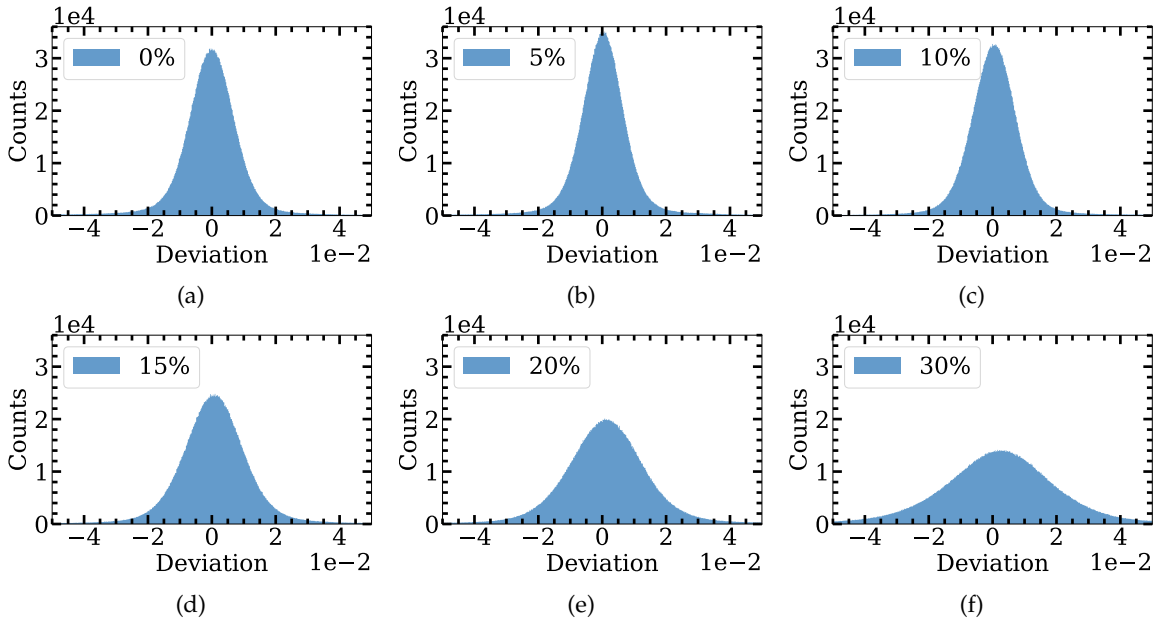


Figure 20: The deviation of the normalised average of the reconstructed objects from the initial object for all the intensity reduction parameters. The normalisation was done by dividing each mean reconstruction with their respective μ_h value, which can be found in Table 4.

The deviation distributions have also been fitted with Gaussian functions, and the parameters are listed in Table 5. Again, the standard deviation of the distributions increased with increasing intensity reductions.

Table 5: Mean and standard deviation of the deviation distributions for different intensity reduction parameters. All the values are given in arbitrary units. Compared to the raw data shown in Figure 20, the values have been divided by 10^4 , 10^3 and 10^2 , respectively.

Int. red.	a	μ	σ
0%	3.12	0.05	0.70
5%	3.42	0.25	0.63
10%	3.20	0.45	0.68
15%	2.41	0.64	0.91
20%	1.94	1.22	1.13
30%	1.35	2.26	1.62

5.5 FURTHER WORK

This project has proved that there might be significant negative consequences of Bragg scattering in CDI experiments, given that the amount of scattered photons is sufficiently large. Whether the intensity reductions that have been applied in this project are realistic is a question for further work, and it should be answered before drawing any conclusions.

To get an estimate of the actual intensity reduction, the intensity in the forward direction detector and the intensity measured in the wide angle detector could be compared. It is however not straight forward to compare these numbers. In the forwards direction, a so-called beamstop blocks the most intensive parts of the beam to protect the detector. Additionally, the wide angle detector only covers a small solid angle, which would not necessarily be representative for the total intensity scattered to wider angles. Hence, one can neither determine how much of the incoming beam that is hitting the forward detector, nor decide how much is scattered. Therefore is it challenging to compare the intensity measurement in the small angle and wide angle regime. A possible solution is to numerically calculate the diffraction pattern of a digital reconstruction of a real sample, and compare this with the measured diffraction pattern. Then one could try to match the parts unaffected by the beamstop and other experimental defects. Thereafter, the calculated diffraction pattern could be scaled according to the measured one and the total intensity in the forward direction could be estimated. If the total intensity which the sample was exposed with is known as well, a reasonable estimate on the intensity reduction could be made. Additionally, an estimate on how much of the intensity that is scattered to wider angles could be made by averaging the measured wide angle signal over a large set of experimental data.

It would also be interesting to perform the aforementioned calculations for one amorphous and one crystalline sample, to see if any differences in the forward scattering intensities can be found, and thus determine the effect of the crystallinity of the sample. The expected result would be that the amorphous sample would have a stronger signal in the forward direction. Whether this could be found or not, and whether this potential difference would be of significant magnitude, would be interesting to explore. If a sufficiently large difference were found, i.e. in the order of the reductions that have been applied in this project, it would support the findings in this report.

Even though a large intensity reduction would have been found in an experiment similar to the one outlined above, it would not necessarily mean that today's CDI results could not be trusted. This project has only explored the effects of Bragg scattering in a very limited parameter space. Before drawing any conclusions there are multiple other factors that would have to be considered. It would for example be of interest to see if different reconstruction algorithms would be able to handle the intensity reductions better. For this project, other algorithms have not been examined in detail because of lack of time, but it is likely that it could have affected the results.

A further study should also include the analysis of different object, both varying in shape and size, but more importantly in their crystallinity. In this project, the sample was assumed to consist of two intersecting single crystals. This is seldom the case in real experiments. If a crystalline sample is analysed using CDI, it is usually polycrystalline. To study this The author expects the effects of Bragg scattering to be smaller for polycrystalline samples, as the effect per scattering plane is smaller. At the same time, the Bragg condition is likely to be fulfilled more often, and it would be more difficult to take all the different reductions into account in a potential new phase retrieval algorithm. However, due to the smaller amplitude of the reductions, and their random affection on different parts of the diffraction pattern, they can most likely be treated more like normal noise, which the reconstruction algorithms already handle quite elegantly, as described in Section 3.4.

Finally, it would be interesting to see if the results of this project could be reproduced. For example by using a single crystal sample twice. Once with a orientation where the Bragg diffraction condition would be fulfilled, and once with an orientation where it would not, or at least to a lower degree. Then, the reconstruction quality of the two orientations could be compared. If the quality of the reconstruction were significantly worse for the orientation where the Bragg condition was fulfilled, this would suggest that Bragg scattering do have a significant effect on the reconstruction quality, as the results of this project indicate.

6

CONCLUSION

During the course of this project, a clear connection between an decreasing reconstruction quality and an increasing amount of Bragg scattering in a CDI process has been demonstrated. By numerically calculating the diffraction pattern of a digitally constructed sample, applying an intensity reduction for some projections, before reconstructing the sample again and comparing it against the initial object, it has been shown that the local density deviations can increase significantly. Additionally, with a sufficiently large intensity loss due to Bragg scattering, the phase retrieval algorithms used in this project failed to reconstruct the sample. This indicates that Bragg scattering might have an effect on the reconstruction process. However, it must be noted that the assumed intensity reductions have not been compared against actual intensity losses in real experiments. Additionally, the parameter space used in the reconstruction process of this project has been very limited. Therefore, a further analysis, both comparing the intensity reductions applied in this project with measured intensity reductions and exploring the use of different reconstruction algorithms, have to be performed before drawing any final conclusions.

BIBLIOGRAPHY

- [1] J. Als-Nielsen and D. McMorrow. *Elements of Modern X-ray Physics*. 2nd. Chichester, West Sussex, UK: John Wiley & Sons, Ltd, 2011.
- [2] R. H. T. Bates and W. R. Fright. "Composite two-dimensional phase-restoration procedure." In: *J. Opt. Soc. Am.* 73.3 (1983), pp. 358–365.
- [3] R. H. T. Bates and W. R. Fright. "Two-Dimensional Phase Restoration." In: *Fourier Techniques and Applications*. Ed. by John F. Price. Boston, MA: Springer US, 1985, pp. 121–148.
- [4] R.H.T Bates. "Fourier phase problems are uniquely soluble in more than one dimension. I: underlying theory." In: *Optik* 61 (1982), pp. 247–262.
- [5] R.H.T Bates. "Uniqueness of solutions to two-dimensional fourier phase problems for localized and positive images." In: *Comput. Gr. Image Process.* 25.2 (1984), pp. 205–217.
- [6] W. H. Bragg and W. L. Bragg. "The reflection of X-rays by crystals." In: *Proc. R. soc. Lond. Ser. A-Contain. Pap. Math. Phys. Character* 88.605 (1913), pp. 428–438.
- [7] Y. M. Bruck and L. G. Sodin. "On the ambiguity of the image reconstruction problem." In: *Opt. Commun.* 30.3 (1979), pp. 304–308.
- [8] H. N. Chapman and K. A. Nugent. "Coherent lensless X-ray imaging." In: *Nat. Photon* 4.12 (2010), pp. 833–839.
- [9] B. Chattopadhyay, A. S. Madathiparambil, F. K. Mürer, P. Cerasi, Y. Chushkin, F. Zontone, A. Gibaud, and D. W. Breiby. "Nanoscale imaging of shale fragments with coherent X-ray diffraction." In: *J. Appl. Crystallogr.* 53.6 (2020), pp. 1562–1569.
- [10] T. Ekeberg et al. "Three-Dimensional Reconstruction of the Giant Mimivirus Particle with an X-Ray Free-Electron Laser." In: *Phys. Rev. Lett.* 114 (9 Mar. 2015), pp. 098–102.
- [11] V. Favre-Nicolin, J. Coraux, M. Richard, and H. Renevier. "Fast computation of scattering maps of nanostructures using graphical processing units." In: *J. Appl. Crystallogr.* 44.3 (2011), pp. 635–640.
- [12] V. Favre-Nicolin, G. Girard, S. Leake, J. Carnis, Y. Chushkin, J. Kieffer, P. Paleo, M. Richard, et al. "PyNX: high-performance computing toolkit for coherent X-ray imaging based on operators." In: *J. Appl. Crystallogr.* 53.5 (2020), pp. 1404–1413.
- [13] J. R. Fienup. "Reconstruction of an object from the modulus of its Fourier transform." In: *Opt. Lett.* 3.1 (1978), pp. 27–29.
- [14] J. R. Fienup. "Phase retrieval algorithms: a comparison." In: *Appl. Opt.* 21 (Aug. 1982), pp. 2758–2769.
- [15] J. R. Fienup. "Reconstruction of a complex-valued object from the modulus of its Fourier transform using a support constraint." In: *J. Opt. Soc. Am. A* 4.1 (1987), pp. 118–123.
- [16] J. R. Fienup and C. C. Wackerman. "Phase-retrieval stagnation problems and solutions." In: *J. Opt. Soc. Am. A* 3.11 (1986), pp. 1897–1907.
- [17] R. W. Gerchberg and W. O. Saxton. "A practical algorithm for the determination of phase from image and diffraction plane pictures." In: *Optik* 35.2 (1972), pp. 237–246.
- [18] R. W. Gerchberg and W. O. Saxton. "Comment on 'A method for the solution of the phase problem in electron microscopy'." In: *J. Phys. D: Appl. Phys.* 6.5 (1973), p. L31.

- [19] M. Guizar-Sicairos and J. R. Fienup. "Understanding the twin-image problem in phase retrieval." In: *J. Opt. Soc. Am. A* 29.11 (2012), pp. 2367–2375.
- [20] M. Hayes. "The reconstruction of a multidimensional sequence from the phase or magnitude of its Fourier transform." In: *IEEE Trans. Acoust* 30.2 (1982), pp. 140–154.
- [21] M. Holler, M. Guizar-Sicairos, E. H. R. Tsai, et al. "High-resolution non-destructive three-dimensional imaging of integrated circuits." In: *Nature* 543 (2017), pp. 402–406.
- [22] I. Juvells, S. Vallmitjana, A. Carnicer, and J. Campos. "The role of amplitude and phase of the Fourier transform in the digital image processing." In: *American Journal of Physics* 59.8 (1991), pp. 744–748.
- [23] T. Latychevskaia. "Iterative phase retrieval in coherent diffractive imaging: practical issues." In: *Appl. Opt.* 57.25 (2018), pp. 7187–7197.
- [24] S. Marchesini, H. He, H. N. Chapman, S. P. Hau-Riege, A. Noy, M. R. Howells, U. Weierstall, and J. C. H. Spence. "X-ray image reconstruction from a diffraction pattern alone." In: *Phys. Rev. B* 68 (14 2003), p. 140101.
- [25] J. Miao, P. Charalambous, J. Kirz, and D. Sayre. "Extending the methodology of X-ray crystallography to allow imaging of micrometre-sized non-crystalline specimens." In: *Nature* 400.6742 (1999), pp. 342–344.
- [26] J. Miao, T. Ishikawa, I. K. Robinson, and M. M. Murnane. "Beyond crystallography: Diffractive imaging using coherent x-ray light sources." In: *Science* 348.6234 (2015), pp. 530–535.
- [27] J. Miao, R. L. Sandberg, and C. Song. "Coherent X-Ray Diffraction Imaging." In: *IEEE J. Sel. Top. Quantum Electron.* 18.6742 (2012), pp. 399–410.
- [28] J. Miao, D. Sayre, and H. N. Chapman. "Phase retrieval from the magnitude of the Fourier transforms of nonperiodic objects." In: *J. Opt. Soc. Am. A* 15.6 (1998), pp. 1662–1669.
- [29] T. Narayanan, M. Sztucki, P. Van Vaerenbergh, J. Léonardon, J. Gorini, L. Claustre, F. Sever, J. Morse, and P. Boesecke. "A multipurpose instrument for time-resolved ultra-small-angle and coherent X-ray scattering." In: *J. Appl. Crystallogr.* 51.6 (2018), pp. 1511–1524.
- [30] H. Nyquist. "Certain Topics in Telegraph Transmission Theory." In: *Trans. AIEE* 47.2 (1928), pp. 617–644.
- [31] A.V. Oppenheim and J.S. Lim. "The importance of phase in signals." In: *Proc. IEEE* 69.6 (1981), pp. 529–541.
- [32] F. Pfeiffer. "X-ray ptychography." In: *Nat. Photon* 12.1 (Jan. 2018), pp. 9–17.
- [33] J. M. Rodenburg, A. C. Hurst, A. G. Cullis, B. R. Dobson, F. Pfeiffer, O. Bunk, C. David, K. Jefimovs, and I. Johnson. "Hard-X-Ray Lensless Imaging of Extended Objects." In: *Phys. Rev. Lett.* 98 (3 2007), p. 034801.
- [34] T. Salditt and M. Osterhoff. "X-ray Focusing and Optics." In: *Nanoscale Photonic Imaging*. June 2020, pp. 71–124.
- [35] D. Sayre. "Some implications of a theorem due to Shannon." In: *Acta Cryst.* 5 (1952), p. 843.
- [36] C.E. Shannon. "Communication in the Presence of Noise." In: *Proc. IRE* 37.1 (1949), pp. 10–21.
- [37] Y. Takahashi, Y. Nishino, R. Tsutsumi, N. Zettsu, E. Matsubara, K. Yamauchi, and T. Ishikawa. "High-resolution projection image reconstruction of thick objects by hard x-ray diffraction microscopy." In: *Phys. Rev. B* 82 (21 2010), p. 214102.

- [38] F. van der Veen and F. Pfeiffer. "Coherent x-ray scattering." In: *J. Phys. Condens. Matter.* 16.28 (2004), p. 5003.
- [39] A. Vretblad. *Fourier Analysis and Its Applications*. 1st. New York, NY: Springer, 2010.
- [40] E. T. Whittaker. "On the Functions which are represented by the Expansions of the Interpolation-Theory." In: *Proc. R. Soc. Edinb* 35 (1915), 181–194.
- [41] G. J. Williams, M. A. Pfeifer, I. A. Vartanyants, and I. K. Robinson. "Three-Dimensional Imaging of Microstructure in Au Nanocrystals." In: *Phys. Rev. Lett.* 90 (17 2003), p. 175501.
- [42] P. Willmott. *Introduction to Synchrotron Radiation*. 1st. Chichester, West Sussex, UK: John Wiley & Sons, Ltd, 2011.
- [43] J. Wu and J. Spence. "Reconstruction of complex single-particle images using charge-flipping algorithm." In: *Acta cryst.* 61 (Apr. 2005), pp. 194–200.
- [44] G. Xiong, O. Moutanabbir, M. Reiche, R. Harder, and I. Robinson. "Coherent X-Ray Diffraction Imaging and Characterization of Strain in Silicon-on-Insulator Nanostructures." In: *Adv. Mater.* 26.46 (2014), pp. 7747–7763.